

# Reynolds-number effects on the structure of a turbulent channel flow

By T. WEI† AND W. W. WILLMARTH

Department of Aerospace Engineering, The University of Michigan, Ann Arbor, MI 48109, USA

(Received 9 April 1987 and in revised form 23 July 1988)

A high resolution, two component laser-Doppler anemometer has been used for turbulence measurements at a high data rate in a channel flow of water. Measurements of the velocity components in the stream direction and in a direction normal to the wall are reported over the Reynolds number range of 3000–40 000. The combination of high spatial resolution and high data rates enabled accurate reconstruction of time dependent velocity traces. Long-time statistical averages of these signals clearly show that profiles of the dimensionless turbulence quantities such as turbulence intensities and Reynolds stress are strongly Reynolds-number dependent over a large part of the channel flow. For instance, in the Reynolds-number range of this investigation, it is shown that the fluctuating turbulence quantities do not scale with wall variables even as close as 15 viscous lengths from the wall. The velocity traces and associated power spectra exposed two phenomena which may explain the Reynolds number dependencies.

## 1. Introduction

This paper is a report of laser-Doppler anemometer (LDA) velocity measurements made in turbulent channel flows over the range,  $3000 \leq Re \leq 40\,000$ . (The notation denotes a Reynolds number based on centreline velocity and half channel width.) The purpose of the investigation is to test the validity of the inner scaling laws in this range. Attention will be paid to the effect of Reynolds number on the small-scale structures in the inner region.

It has been experimentally observed that the mean velocity profiles in turbulent wall bounded flows can be divided into outer and inner regions. In general, the outer region of a channel flow is located in the central portion of the channel and the flow is controlled primarily by inertial forces. Although the outer region is influenced by the effects of the wall, the structure of the flow tends to be more wake-like in character. The significant parameters are the centreline velocity, friction velocity, and the half-channel thickness, the so-called ‘outer variables’. Adjacent to the channel walls, the flow is dominated by viscous forces. This is the part of the flow that is significantly affected by the presence of the solid surface. Here the ‘inner variables’, the kinematic viscosity and the friction velocity, are important.

The classic idea of inner scaling is that if one were to measure a number of profiles of a particular turbulence quantity at different Reynolds numbers, (say, for example, the root-mean-square of the velocity fluctuations) then each of the profiles, when non-dimensionalized using inner variables, should collapse onto a single curve. This should hold true for all of the turbulence quantities (e.g. mean velocity, r.m.s.-

† Present address: Rutgers University, PO Box 909, Piscataway, NJ 08855–0909, USA.

velocity fluctuations, Reynolds stress, power spectra). Inner scaling holds that there should be a single, Reynolds-number independent, non-dimensional profile for each of these turbulence quantities. The results of this investigation demonstrate that inner scaling is not valid in the Reynolds number range,  $3000 \leq Re \leq 40\,000$ .

### 1.1. *A review of the turbulent channel flow literature*

Inner scaling of the mean streamwise velocity in the near-wall region of plane-wall bounded turbulent flows is well documented. Excellent review articles were written by Clauser (1956), and Coles (1956) for turbulent boundary-layer flows with zero pressure gradient. Two of the more noteworthy works on turbulent channel flow were Laufer (1950), and Comte-Bellot (1965) over the Reynolds number range of 12 000–230 000. Additional work by Eckelmann (1974) has extended the inner scaling of mean streamwise velocity to Reynolds numbers as low as 2800. However, there has not yet been a rigorous demonstration of the inner scaling of the fluctuating quantities in channel flows.

One of the first attempts to scale fluctuating quantities was made by Laufer (1950). A number of measurements of streamwise turbulence intensity,  $u'$ , including Laufer's, have been compiled in figure 1. Figure 2 presents a compilation of turbulence intensity measurements for the velocity component normal to the wall,  $v'$ . Laufer (1950) discussed the effect of Reynolds number on the inner scaling of streamwise turbulence intensity in the range  $12\,200 < Re < 61\,600$ . It appeared that the peak value of intensity,  $u'/u_\tau$ , decreased with increasing Reynolds number owing to decreasing resolution of his hot-wire probes. Unfortunately, he was not able to determine a length correction for his probes.

Johansson & Alfredsson (1982) also speculated on a Reynolds number effect on the inner scaling of fluctuating quantities. They used hot-film probes in a water channel to examine the Reynolds number range,  $6900 < Re < 24\,450$ . Their  $u'$  data are shown in figure 1. A single  $v'$  profile was reproduced from a later work, Alfredsson & Johansson (1984), and appears in figure 2. Like Laufer (1950), they observed that the profiles of  $u'/u_\tau$  for different Reynolds numbers did not collapse onto a single curve. They left the subject open with an argument that hot wires were inherently unable to make accurate measurements deep inside the inner region.

Comte-Bellot (1965) found no Reynolds-number effect on inner scaling for Reynolds numbers from 57 000 to 230 000. In that range, she found that even the higher-order moments of the streamwise and normal velocities,  $u$  and  $v$ , scale on inner variables out to  $y^+ = 100$ .

Eckelmann (1974) reported on hot-film measurements made in an oil channel over the Reynolds number range,  $2800 < Re < 4100$ . He showed that both  $u'/u_\tau$  and  $v'/u_\tau$  satisfy inner scaling out to  $y^+ = 23$ . He did not show any data beyond that location. His later investigations, Kreplin & Eckelmann (1979), Kastrinakis & Eckelmann (1983), and Johnson & Eckelmann (1983), seem to assume *a priori* an inner scaling for all fully developed turbulent channel flows.

The problem with Eckelmann's first work, Eckelmann (1974), is that the Reynolds number range investigated is very small. The largest Reynolds number is less than 50% greater than the smallest number. It is not clear that this range would be sufficiently large to distinguish any but the strongest Reynolds number trends.

An excellent study, specifically addressing the question of scaling laws in turbulent pipe flows, was written by Perry & Abell (1975). They demonstrated that not only the mean streamwise velocity, but the streamwise and normal fluctuations, Reynolds stress, and power spectra all scale on inner variables in the inner region over the

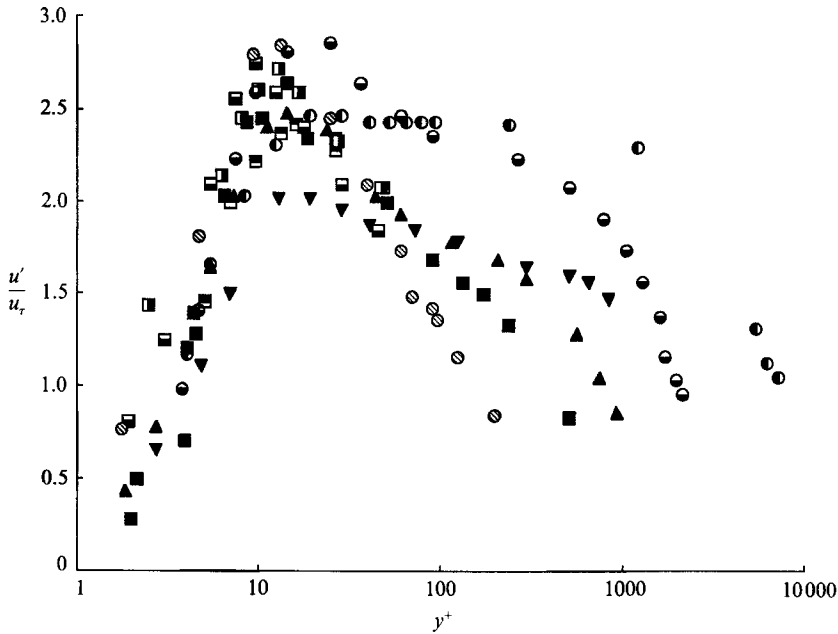


FIGURE 1. Streamwise turbulence intensity profiles, non-dimensionalized with respect to inner variables, taken from the turbulent channel flow literature:  $\odot$ ,  $Re = 3850$  (Kreplin & Eckelmann 1979);  $\square$ ,  $Re = 6900$  (Johansson & Alfredsson 1982);  $\blacksquare$ ,  $Re = 17300$  (Johansson & Alfredsson 1982);  $\blacksquare$ ,  $Re = 24450$  (Johansson & Alfredsson 1982);  $\blacksquare$ ,  $Re = 12300$  (Laufer 1950);  $\blacktriangle$ ,  $Re = 30800$  (Laufer 1950);  $\blacktriangledown$ ,  $Re = 61600$  (Laufer 1950);  $\odot$ ,  $Re = 57000$  (Comte-Bellot 1965);  $\bullet$ ,  $Re = 230000$  (Comte-Bellot 1965).

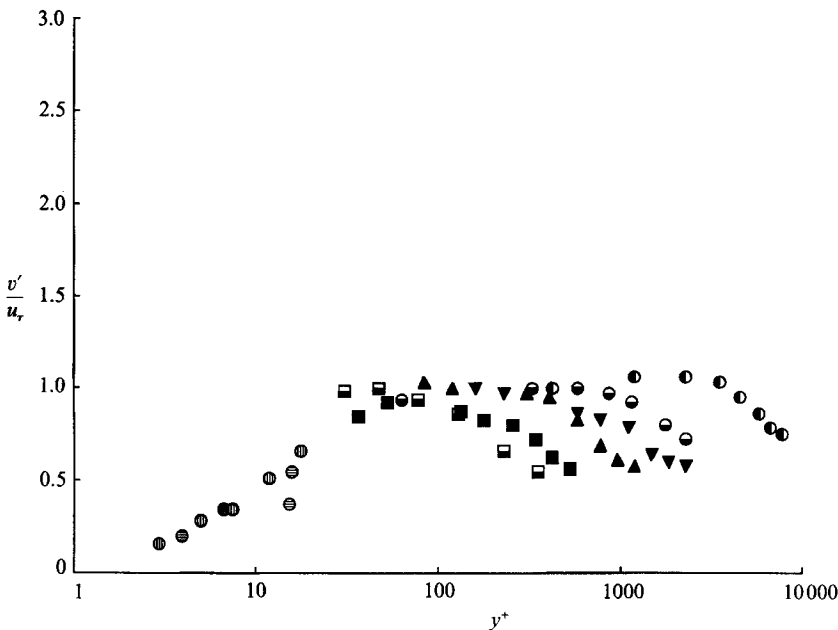


FIGURE 2. Turbulence intensity profiles,  $v'$ , taken from the turbulent channel flow literature:  $\odot$ ,  $Re = 2800$  (Eckelmann 1974);  $\bullet$ ,  $Re = 4100$  (Eckelmann 1974);  $\square$ ,  $Re = 7500$  (Alfredsson & Johansson 1984);  $\blacksquare$ ,  $Re = 12300$  (Laufer 1950);  $\blacktriangle$ ,  $Re = 30800$  (Laufer 1950);  $\blacktriangledown$ ,  $Re = 61600$  (Laufer 1950);  $\odot$ ,  $Re = 57000$  (Comte-Bellot 1965);  $\bullet$ ,  $Re = 230000$  (Comte-Bellot 1965);

Reynolds number range,  $78000 < Re < 260000$ . It may be noteworthy that these Reynolds numbers are higher than those of all other studies cited above, except for Comte-Bellot (1965). Comte-Bellot examined an analogous range in channel flows and also found that inner scaling existed. This suggests the existence of a 'critical' Reynolds number above which turbulence quantities in the inner region scale on inner variables. The other works cited in this section may have been conducted below this 'critical' value.

Head & Bandyopadhyay (1981) performed a smoke visualization study of turbulent boundary layers in a wind tunnel. Their investigation covered a Reynolds-number range, based on momentum thickness, of 500–17500. Photographs of the inner regions of the boundary layers clearly show increased vortex stretching with increasing Reynolds number. At high Reynolds numbers, the inner region looks very different from the low-Reynolds-number counterpart. Unfortunately, it is very difficult to extract quantitative information from flow visualization studies. Head & Bandyopadhyay (1981) were not able to establish whether or not the apparent changes in structure scaled on inner variables.

The existence of Reynolds-number effects on the streamwise fluctuations have recently been observed in low-Reynolds-number, zero-pressure-gradient turbulent boundary layers by Purtell, Klebanoff & Buckley (1981) and Erm, Smits & Joubert (1985). Both groups of investigators made hot-wire measurements in air over virtually identical Reynolds-number ranges. Purtell *et al.* (1981) examined the Reynolds-number range, based on momentum thickness 465–5100; Erm *et al.* (1985) covered the range, 617–5010. Both sets of data clearly show that  $u'/u_\tau$  rapidly increases from zero at the wall, reaches a maximum value around  $y^+ = 12$ , and decreases back toward zero in the free stream. The  $u'/u_\tau$  profiles exhibit a clear Reynolds-number dependence for  $y^+ > 12$ ;  $u'/u_\tau$  decreases less rapidly with increasing Reynolds number. Thus, the turbulence intensity peak is broader at higher Reynolds numbers. There is evidence in Purtell's data that the magnitude of the intensity peak may increase with Reynolds number as well. Neither study speculates on the cause of these effects.

To date, most investigators of fully developed turbulent channel flows seem to have accepted the idea of inner scaling for all Reynolds numbers and focused attention on the structure of the inner region; much research has centred on the existence of hairpin vortices as the fundamental structure in the inner region. Consequently, there really has been no verification of the inner scaling of the fluctuating quantities. This is more than an academic problem because a great deal of the current quantitative work on coherent structures deals with the scaling properties of these structures.

An example of this problem is the disagreement between the conclusions of Willmarth & Bogar (1977) and those of Johnson & Eckelmann (1983). Willmarth & Bogar (1977) developed very small X-array hot-wire probes to measure small-scale structures in the inner region of a turbulent boundary layer in a wind tunnel. At a Reynolds number based on momentum thickness of 11700, the size of the probes was approximately 2.5 viscous lengths. They calibrated their probes by recording the signals produced in steady flow for a wide range of probe angles of inclination and flow speeds. When the probes were placed in the boundary-layer flow, very close to the wall, they observed signals which fell well outside the calibration curves. They concluded that these signals could only be caused by small-scale shear layers striking the probes; the strong shear layer present in a small intense vortex would cause one

wire to sense one velocity vector while the second wire sensed a completely different vector.

Johnson & Eckelmann (1983) attempted to reproduce the Willmarth & Bogar (1977) experiment in an oil channel. They scaled their hot-film probes on inner variables to match the Willmarth & Bogar probes. The Reynolds number of the Johnson & Eckelmann (1983) flow was 3800 based on centreline velocity and half-channel width. They did not detect any irregular signals and concluded that vibration of the probes used by Willmarth & Bogar was responsible for signals outside the calibration range. Outside of the fact that the flow geometries were different, one was a boundary layer and the other was a fully developed channel flow, the Reynolds numbers were very different. To make the comparison between the two flows, Johnson & Eckelmann (1983) had to have implicitly assumed that a scaling of the inner region existed between the two flows.

It is believed that the primary reason the inner scaling of channel flows have never been adequately demonstrated is the difficulty in making good measurements. Recently, a number of studies have shown that the effect of probe size is very important in the detection of small-scale inner structures. Johansson & Alfredsson (1983), Blackwelder & Haritonidis (1983), and Luchik & Tiederman (1986) have found that turbulence intensity measurements made with oversized (relative to the smallest significant eddies) hot-film and LDA probes show a lack of resolution. Schewe (1983) noted a similar trend with pressure fluctuation measurements using surface mounted pressure transducers.

A probe essentially integrates over the length, area, or volume of the active sensing element. That is, the signal from the probe represents the average value over the entire sensor. Large-amplitude signals from disturbances much smaller than the sensor will be attenuated by the averaging process. Attenuation of these peaks leads directly to measured intensity values which are too small.

Laufer (1950) observed that the peak value of  $u'/u_\tau$  decreased with increasing Reynolds number but was not able to determine a length correction for his hot-wire probes. His non-dimensional probe length increased from 3 viscous lengths at  $Re = 12300$  to 13 viscous lengths at  $Re = 61600$ . This fourfold loss in spatial resolution probably contributes greatly toward explaining the reduction in the streamwise intensity peak. It also suggests the existence of important turbulent structures which are smaller than 10 viscous lengths in size.

A similar trend can be seen in the streamwise intensity peak from Comte-Bellot (1965). Although she claimed that her fluctuating profiles scaled with inner variables, examination of her data shows a systematic decrease in the peak value of  $u'/u_\tau$  from a value of approximately 2.85 at the  $Re = 57000$ , down to 2.65 at  $Re = 120000$ , and finally to 2.5 at  $Re = 230000$ . The highest and lowest Reynolds-number data are shown in figure 1. In the Reynolds-number range examined by Comte-Bellot, the dimensionless probe length increased from 13 to 36 viscous lengths. This result was not noted by Comte-Bellot.

## 1.2. Objectives

There is clearly a need for a set of high-resolution measurements in the inner region of turbulent channel flows for low to moderately high Reynolds numbers. These measurements will confirm or deny the existence of inner scaling in that range. The feasibility of making such measurements with an LDA was verified by Willmarth & Velazquez (1983). Willmarth & Velazquez (1983) constructed a two-component LDA

system with a measurement volume which was roughly a cube, 50  $\mu\text{m}$  on a side. They made a single run in a turbulent channel flow at a Reynolds number of 14 700. Their initial study was limited because the data rates obtained were too low to reconstruct the time dependent velocity signals accurately.

The first objective of the present investigation is to test for the existence of an inner scaling law for turbulent channel flows in the range,  $3000 < Re < 40\,000$ . This entails acquiring accurate, simultaneous, time dependent records of velocity components in the streamwise direction and the direction perpendicular to the wall. This will provide measurements of turbulence intensities, Reynolds stress, and power spectra to a degree of resolution unattainable with conventional anemometry techniques.

If inner scaling does not hold over this range (i.e. there is a Reynolds-number effect), an argument will be made that there is an evolution from low-Reynolds-number fully developed turbulent channel flow to high-Reynolds-number turbulent channel flow. A rationale supporting the existence of a Reynolds-number dependent evolution begins with the idea that a laminar flow has no Reynolds stress. However, a turbulent flow at large Reynolds number has a Reynolds-stress profile, the maximum value of which, non-dimensionalized on the friction velocity, approaches unity. It is not clear that turbulence behaves as a 'digital' process whereby the normalized Reynolds stress is either zero or unity. It is hypothesized that there must be some Reynolds-number range where the turbulence 'evolves' to the high Reynolds-number turbulence state. The second objective of this investigation is to develop insight into this evolutionary process.

## 2. Apparatus

### 2.1. Water channel facility

A closed-circuit water channel, consisting of a free-surface reservoir, pump, channel, and downstream pressure weir, was built for this investigation. The design was patterned on the channel used by Willmarth & Velazquez (1983) and is shown schematically in figure 3. A detailed description of the system was written by Wei (1987).

The pump was operated at both 1800 and 3600 r.p.m. using two different motors. The flow rate through the test section was further regulated at the pump exit by a bypass circuit with two valves, as illustrated in figure 3. Wherever possible, 10.16 cm diameter piping was used throughout the system because its cross-sectional area matched that of the test section.

Flow entered the upstream end of the settling chamber along the centreline of the channel test section. Two stainless steel perforated plate screens were placed inside the settling chamber to break up the large eddies generated at the inlet. Before entering the test section, the flow passed through a converging plane-walled contraction. This eliminated the large counter-rotating vortices, associated with a Borda type entrance. The contraction, however, did not completely eliminate turbulence at the test-section inlet which aided in establishing a fully developed turbulent profile.

The channel test-section dimensions were 2.572 cm wide, 30.48 cm high, and 254 cm long. The measuring station was located 222.25 cm downstream of the test-section inlet. At the time of assembly, the channel width was made to be constant to within 0.25 % along its entire length. Similarly, the channel height was constant to within 0.04 %. To maintain uniform width, six clamps were applied along the



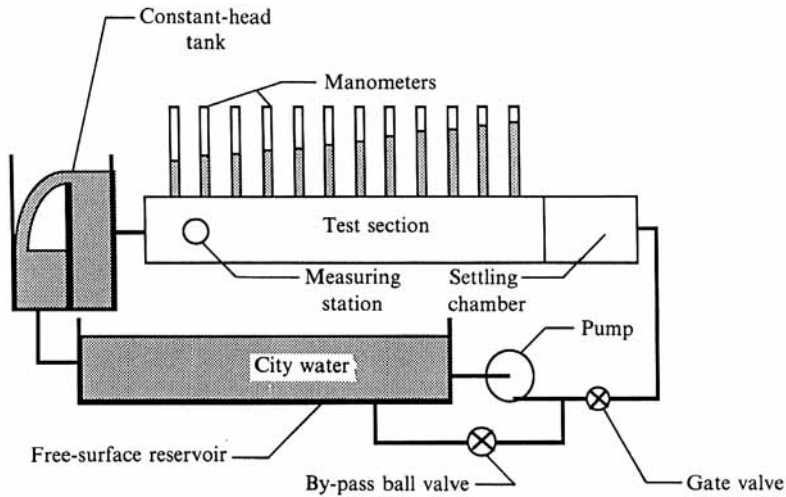


FIGURE 3. Schematic diagram of the closed-circuit flow loop.

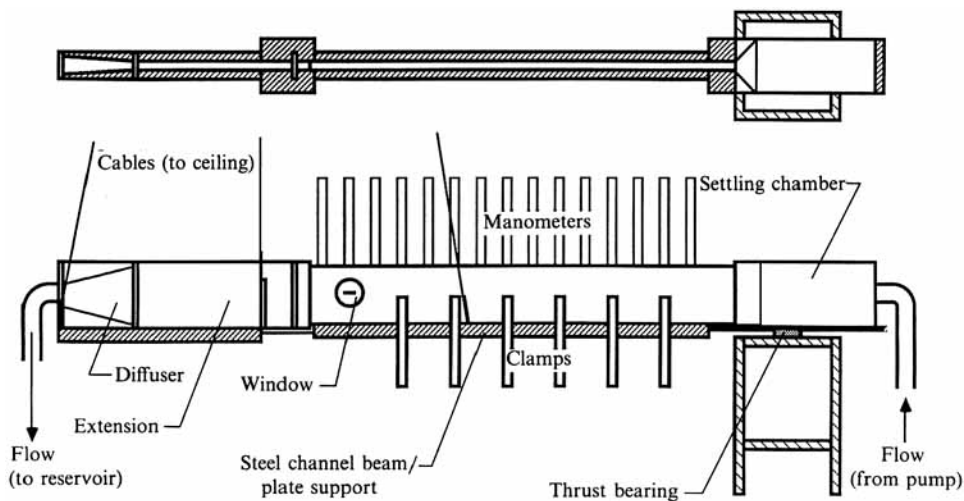


FIGURE 4. Detailed top- and side-view drawings of the channel test section.

centreline of the test section at 30.48 cm intervals, as shown in figure 4. The test-section walls were made from two sandwich construction panels consisting of a 'Klegecell' foam core wrapped in 0.159 cm thick stainless steel sheet. There were no scratches larger than those left by a light buffing with steel wool. The panels were separated by two 2.54 cm wide stainless steel spacer bars and bolted together at 15.24 cm intervals. A schematic assembly drawing of the test section, including settling chamber, and exit adaptor, is shown in figure 4.

The test section was fitted with fifteen manometers, equally spaced at 15.24 cm intervals, which aided in monitoring the flow in the channel and determining the wall shear stress. The first manometer was placed 198.12 cm upstream of the measuring station. Each pressure tap was 0.14 cm in diameter, drilled into the centreline of the upper spacer bar. The manometers were made of precision bored glass tube, with outside diameter of 3.81 cm and approximate wall thickness of 0.24 cm. In this

manner it was possible to make mean static pressure measurements which were relatively free from the turbulent pressure fluctuations in the channel.

A 91.44 cm long extension was added to the downstream end of the test section. This addition was necessary to keep the measuring station free of exit conditions. Flow passed from the extension into a 10.16 cm diameter pipe via a straight-walled exit adaptor. The intent was to make the flow transition from the rectangular test section to the circular pipe as smooth as possible. The pipe completed the flow loop back to the reservoir.

A T-connection in the return pipe led to a cylindrical downstream constant head tank. For the lower Reynolds-number measurements, the tank was needed to establish a sufficiently high pressure in the test section. The tank was 60.96 cm in diameter, and 152.4 cm deep. A variable-height weir divided the tank into two parts. By blocking the direct line from the test section to the reservoir, flow was diverted into one partition of the tank. Water overflowed the weir into the other partition and returned to the reservoir.

## 2.2. Measuring station

An LDA with four laser beams intersecting at a single point was used to measure the streamwise and perpendicular velocity components in the test section. A detailed description of the LDA appears in §2.3. The measuring station, defined as the streamwise location of the beam crossing, was located 222.25 cm downstream of the test-section inlet. Figure 5 is a top view diagram of the measuring station.

The beams entered the test section through a 5.08 cm long, 0.635 cm high slot, centred about the measuring station. This enabled measurements to be made from the channel near wall to slightly past the centreline. The slot was covered with an extremely thin window of heat shrink Mylar film which was firmly cemented to the plate. The film was 0.00165 cm thick, prior to heat shrinking. The extreme thinness of the film virtually eliminated refraction of the beams by the window. A similar window was installed in the panel on the opposite side of the test section to allow the incident laser beams to exit the channel. This improved the signal-to-noise ratio of the LDA measurements by reducing the amount of ambient light in the vicinity of the measuring volume.

To minimize beam refraction in the path between the laser source and the measuring station, an 'optical head' was used. It was first devised by Willmarth & Velazquez (1983), and is illustrated in figure 5. Two glass windows, in the shape of sections of a spherical shell approximately 10 cm inner radius, were mounted in a triangular brass chamber (the optical head). The optical head was bolted to the optical bench and connected to the channel by a flexible rubber diaphragm and filled with distilled water. When properly aligned, the laser beams passed without refraction through the optical head, perpendicular to the 'spherical' windows, into the test section. The scattered light from the measuring volume also passed outward without refraction.

The optical head was also used to balance the pressure exerted on the Mylar film by the water in the test section (i.e. it prevented deflection of the Mylar film). The 'false head', also shown in figure 5, was designed to make this pressure balance self regulating. The false head was a rectangular box whose projected area, facing the test section, matched that of the optical head. It was placed directly opposite the optical head.

The false head was open at one end and divided into two compartments by a flexible rubber diaphragm. It was rigidly mounted to a fixed steel frame and attached



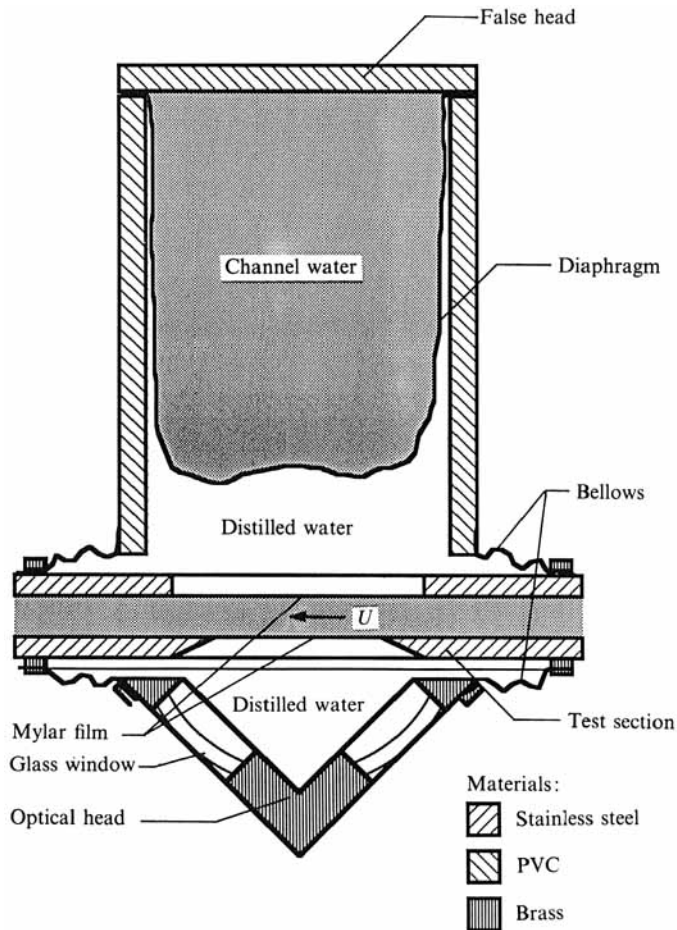


FIGURE 5. Top-view schematic of the measuring station including: Mylar window, optical head and false head.

to the channel in the same manner as the optical head. A tube connected the optical head to one compartment of the false head, and a second tube connected the test section (at the bottom, directly below the measuring station) to the other compartment. Manometers were installed to monitor the pressure in the different compartments.

Distilled water was placed into one compartment of the false head. This was divided between the false head and the optical head through the connecting tube. The second compartment of the false head was automatically filled with water from the test section, via the second connecting tube. Because the test-section water in the false head and the distilled water in the false head were separated by a flexible membrane, the pressures in both compartments would necessarily balance. In this manner, the pressures in the test section, the optical head, and the false head were balanced; there was no net force acting on the Mylar film. In addition, there was no net force pushing or twisting the test section.

When making measurements at different distances from the wall, the test section was positioned relative to the laser beams. This was done because the alignment of the beams was highly sensitive. To do this the entire settling chamber, test section,

exit adaptor assembly was placed on a steel channel beam, as shown in figure 4. The upstream end of this beam was supported by a thrust bearing located underneath the settling chamber. The bearing was mounted on a steel platform which was firmly bolted to the laboratory floor. The downstream end of the channel beam was suspended from the laboratory ceiling, 53.34 cm downstream of the measuring station.

A 'uni-slide' micropositioner was mounted to the false head. Two dial gauges were bolted to the optical bench 19.7 cm downstream of the measuring station. The gauges were placed at different heights and were used to verify that the test section did not twist. It was possible to position the test section relative to the measuring station with an accuracy of better than 0.00254 cm.

### 2.3. Laser Doppler anemometer

A high-resolution, two-colour, two-component LDA was developed for this investigation as an improvement over the system used by Willmarth & Velazquez (1983). The light source was a Spectra-Physics Model 164-08 argon-ion laser. It was generally operated at an all-lines output power of 0.6 W. Both the laser and optics were rigidly mounted on benches which were bolted to the laboratory floor.

To make velocity measurements, the laser beam was split into two pairs of beams which were made to intersect at the measuring station. Two green beams, 514.5 nm wavelength, were used to measure the component of velocity  $45^\circ$  away from the wall (hereinafter referred to as  $U_2$ ), and a pair of blue beams, 488 nm wavelength, measured the velocity component  $45^\circ$  toward the wall (hereafter referred to as  $U_1$ ). A schematic diagram showing the paths of the laser beams from the laser to the measuring station appears in figure 6. The two blue beams entered the channel from upstream of the measuring station at angles of  $30^\circ$  and  $60^\circ$  with respect to the channel wall. The green beams enter the channel from downstream of the measuring station also at  $30^\circ$  and  $60^\circ$  to the channel wall.

Prior to entering the channel, the beams passed through the optical head. Mounted on the outside of the optical head were four focusing lenses, shown in figure 6. The lenses had focal lengths of 15.5 cm and were used to create 50  $\mu\text{m}$  diameter waists in each beam at the measuring volume.

The LDA was operated in the side-scatter mode to improve the spatial resolution of the system. This was done by limiting the area of the measuring volume viewed by the receiving optics as explained in the next paragraph. The scattered light from each of the blue and green measurement volumes was collected by two acromat lenses, mounted immediately outside the optical head. The acromat lenses had focal lengths of 12 cm and were used to create images of the measurement volumes at the windows of two RCA-4526 photomultipliers. The magnification factor of the images was six.

The high spatial resolution of the LDA was obtained through the use of two 300  $\mu\text{m}$  diameter pinholes, placed in front of the photomultiplier windows. These pinholes limited the field of view of the photomultiplier at the measurement volume to a cylindrical region, 50  $\mu\text{m}$  in diameter. Thus, the active sensing volumes of the LDA were roughly spherical in shape with diameters of approximately 50  $\mu\text{m}$ .

Titanium dioxide in the rutile crystalline form was used as seed particles for the LDA. The mean diameter of the particles was 3  $\mu\text{m}$ . A concentrated solution of particles was stored in a bucket above the settling chamber. The solution was injected into the settling chamber using gravity feed.

A small slide mechanism was bolted to each photomultiplier housing between the

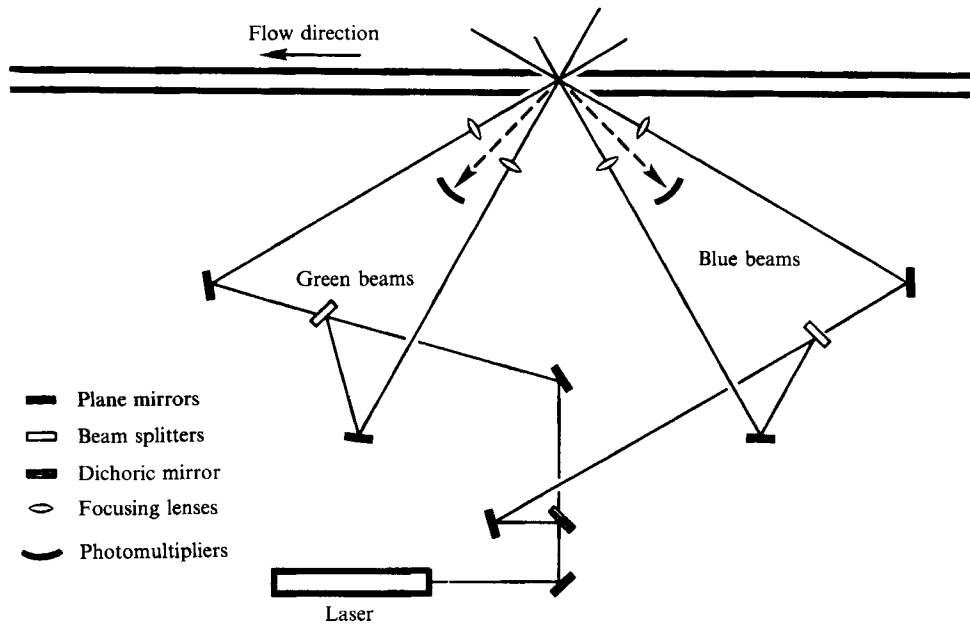


FIGURE 6. Top-view schematic drawing of the laser-beam paths. Note that the beam angles and orientations are correct. However, the lengths are not to scale.

photomultiplier window and the pinhole. The mechanism was fitted with two single-line interference filters, centred at 488 nm and 514.5 nm respectively, mounted side-by-side in a slide. The filters were used to prevent ambient light from striking the photomultiplier detectors and to aid in aligning the LDA. Further details appear in Wei (1987).

Doppler burst detection and processing were accomplished using two Macrodyne Model 2096 laser velocimeter digital burst processors. The Macrodyne burst detection system includes a multi-level sequence test, a 5 count/8 count comparison test and an oversize particle test. For each channel, the photomultiplier signal was pre-amplified by two high-frequency Avantak amplifiers (GPD-461 and GPD-462) connected in cascade. The signal then passed through a Krohn-Hite Model 3103A band-pass filter and into a Macrodyne burst processor. The outputs from the burst processors were subjected to a simultaneity check at the computer interface prior to being stored in permanent files on a Data General NOVA 840 computer. The computer was equipped with a remote terminal in the laboratory as well as a terminal in the computer room, a magnetic tape drive, three hard disc drives each having two megabyte storage capability, a Calcomp plotter, and a high-speed line printer. During data acquisition, the burst signals and analog output signals were monitored on oscilloscopes. The data rate was monitored using a Hewlett-Packard Model 5334A Universal Counter.

### 3. Experimental methods

#### 3.1. Experimental conditions

Four different Reynolds numbers were examined in this investigation, spanning the range from 3000 to 40000. Depending on the Reynolds number, data records were taken at fourteen to twenty different  $y$ -locations between the channel wall and the

channel centreline. A data record consisted of a number of 2048 point data blocks. Each data 'point' included a burst period corresponding to  $U_1$ , a burst period corresponding to  $U_2$ , and time since the last data 'point'. A sufficient number of blocks, calculated from equation 1.100 of Lumley & Panofsky (1964) for the accuracy of statistical time averages, were taken to ensure accurate long-time averages. Details of the calculations appear in Wei (1987).

### 3.2. Data acquisition

For each run, flow in the channel was established and the LDA system was activated. The pressure gradient was visually observed using the glass manometers to ensure that the turbulent flow along the entire test-section length was fully developed. The gradient was also measured for subsequent calculation of the friction velocity.

The channel test section was positioned so that the measurement volume appeared to be in contact with the wall. This was done by moving the channel wall closer and closer to the measurement volume until the LDA no longer detected any Doppler bursts. This was a satisfactory method of establishing an initial estimate of the wall location. The final wall distance measurements, described in the next section, agreed with the initial estimates to within 0.0076 cm. The dial gauge reading corresponding to  $y/b = 0$  was recorded, and the channel was positioned to the  $y$ -location for the first LDA measurements.

At each  $y$ -location, the LDA system was prepared for data acquisition. First, the analog output trace from each burst processor was monitored using a dual beam oscilloscope while the burst processor threshold control for the multi-sequence detection check was varied to obtain the highest possible data rate with a minimum of erroneous samples. The mean value of each analog output trace was monitored using a strip chart recorder to obtain an estimate of the local mean velocity,  $U$ . The Krohn-Hite filters were then adjusted to accept Doppler bursts corresponding to the velocity measurements between 0.2 and 1.8 times the local mean velocity in the  $U_1$  or  $U_2$  direction. The 5/8 comparison check in the burst processor was enabled, and the range setting on the burst processor was adjusted to fully utilize the processors' dynamic range. It should be emphasized that this adjustment process was an iterative procedure because there is a significant interaction between the filter frequency and the signal quality presented to the burst processor. After adjustment of the burst processors the time window of the simultaneity test at the computer interface was set so that the time between the measurements of  $U_1$  and  $U_2$  was slightly less than the time required by a seeding particle to traverse the measurement volume at the local mean speed. After the LDA controls were fixed, the seeding particles were injected into the test section, and the data record was sent to the computer.

### 3.3. Digital signal processing

Figure 7 shows a representative sample of the simultaneous raw data signals,  $U_1$  and  $U_2$ , from the LDA with successive velocity sample pairs randomly spaced in time. The data were taken at a Reynolds number of 14914 at a non-dimensional distance from the wall of  $y^+ = 46$ . The average data rate was 4200 samples per second. The salient feature of the traces in figure 7 is the temporal resolution of the signals.

The next step in the data reduction process was to reproduce the velocity signals at evenly spaced time intervals. The time intervals between reproduced signal points were equal to the average time between data points in the raw signal for that record. The velocities corresponding to each evenly spaced timestep were calculated by linear interpolation between adjacent points in the raw velocity signals.

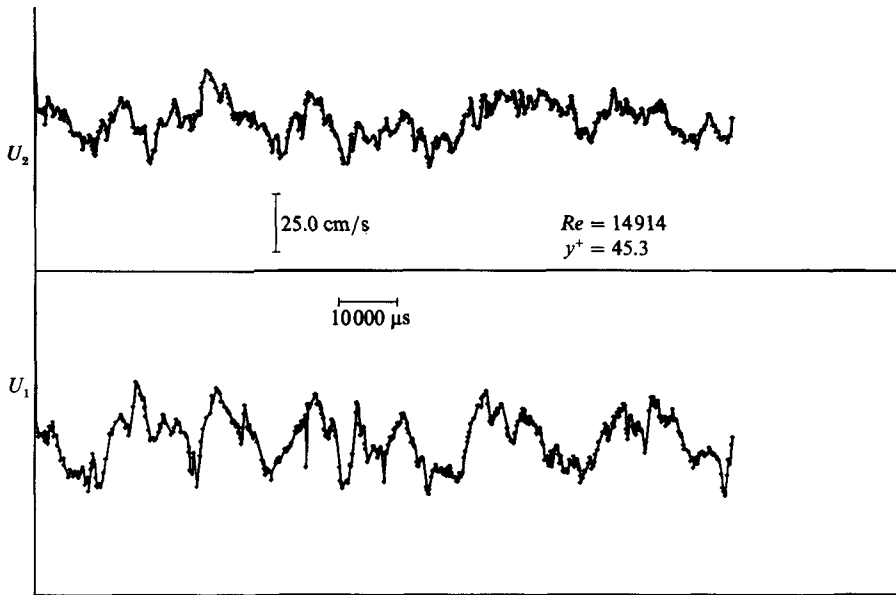


FIGURE 7. Raw time-dependent velocity traces of  $U_1$  and  $U_2$ . Data occur in the figure at random time intervals at an average rate of 4200 samples per second.

These reproduced velocity signals were then filtered and smoothed using a digital Gaussian filter, the third step in the data reduction procedure. The convolution equation for the digital filter was

$$U_{\text{filtered}}(t_m) = \{\sum U_{\text{unfiltered}}(t_n) H(t_m - t_n)\} / \{\sum H(t_m - t_n)\}. \quad (1)$$

The digital filter function,  $H(t_m - t_n)$ , is defined by

$$H(t_m - t_n) = \exp[-\alpha^2(t_m - t_n)^2]. \quad (2)$$

The constant,  $\alpha$ , in the above equation was chosen so that the half-power frequency of the filter function was equal to the viscous angular frequency,  $\omega = 2\pi u_\tau^2/\nu$ , of the channel flow under investigation.

An example of the reproduction/filtering/smoothing process, as applied to the signals in figure 7, is shown in figure 8. It should be noted that the constant,  $\alpha$ , for the filter function used in generating figure 8 was chosen so that the half-power frequency of the filter function was one-sixth of the viscous angular frequency. This was done to better illustrate the effects of the digital filter. A discussion of the frequency response of the digital filter is presented in Wei (1987).

The reproduced/filtered/smoothed  $U_1$  and  $U_2$  signals were then used to generate the time dependent  $U$  and  $V$  velocity traces. Representative samples of these traces are shown in figure 9. These traces were generated from figure 8 by taking the vector sum of  $U_1$  and  $U_2$  to generate  $U$ , and calculating the vector difference to obtain  $V$ . Since the velocity signals were at evenly spaced time intervals, long-time averages could be calculated using ensemble averaging techniques. It was also possible to use these signals to calculate power spectra of the turbulent velocity fluctuations.

The final step in the data reduction procedure was to generate time-dependent Reynolds-stress signals. A representative trace appears in figure 10 created from the traces shown in figure 9. Accurate reconstruction of Reynolds stress traces was possible because of the large signal to noise ratios of the  $U$  and  $V$  signals.



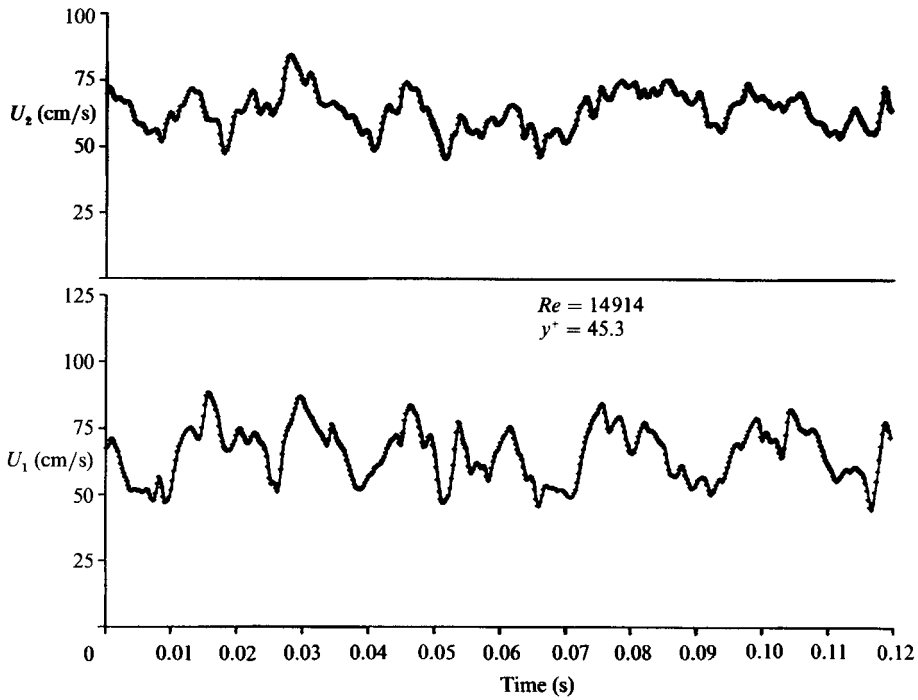


FIGURE 8. Reproduced/filtered/smoothed  $U_1$  and  $U_2$  velocity traces from the data shown in figure 7. Note that the data are now at even time intervals, and much of the noise has been eliminated.

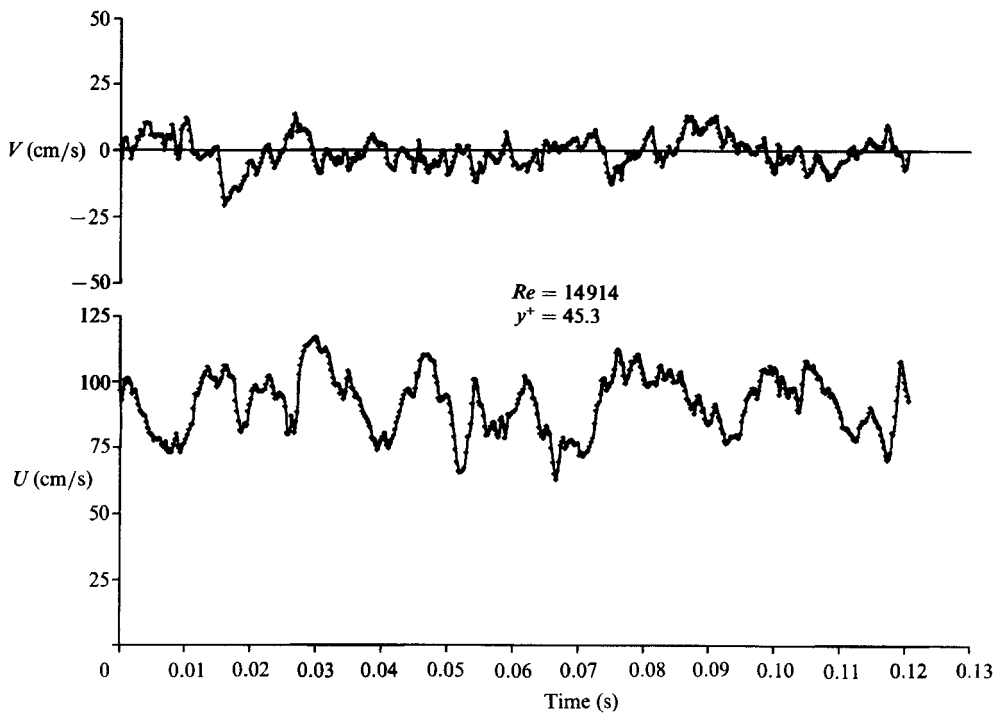


FIGURE 9. Time-dependent  $U$  and  $V$  velocity traces generated from the data shown in figure 8.

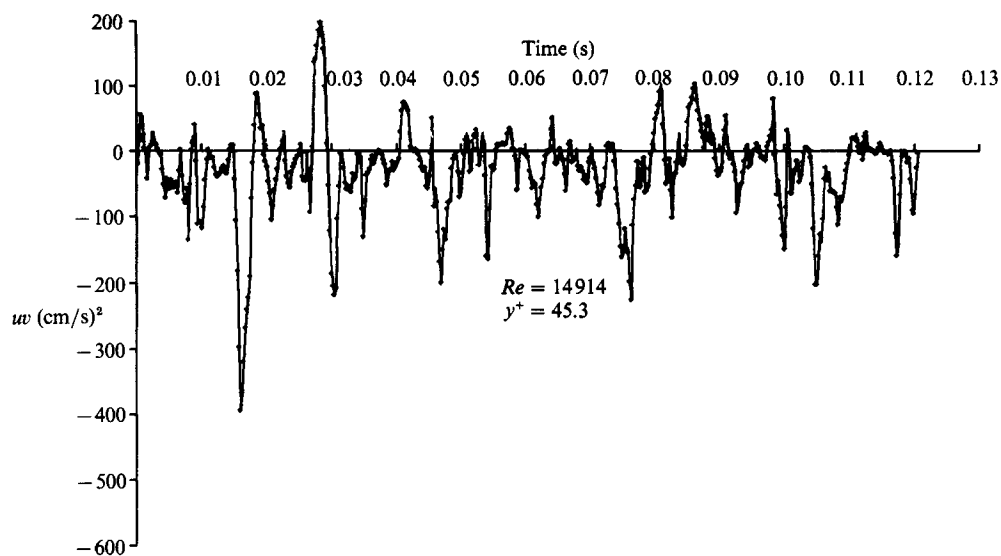


FIGURE 10. Time-dependent Reynolds-stress trace of the data appearing in figure 9.

### 3.4. Temporal resolution and data rates

One of the principal design criteria of the LDA system was that the data rates had to be sufficiently high to accurately reconstruct the time-dependent velocity signals. As explained in this section, the data rates for the lowest three Reynolds numbers were high enough to enable accurate reconstruction of the velocity signals. However, at the highest Reynolds number,  $Re = 39582$ , even the data rate from the LDA was not sufficient to allow accurate reconstruction of the velocity traces.

Before proceeding, it is important to clarify what is meant by 'sufficiently high' data rates. In an ideal LDA, assuming uniform distribution of the seeding particles and very low-amplitude velocity fluctuations, the average data rate increases linearly with velocity, as shown in figure 11. As the speed increases, a proportionally larger number of seeding particles are swept through the measurement volume. For proper operation with a digital burst processor only one particle should be in the LDA measuring volume at any given time. If there is more than one particle in the measuring volume the burst processor will ordinarily detect the faulty burst and will reset without producing a burst period measurement for any of the particles in the measurement volume. Occasionally, the burst processor detection tests will fail and multiple bursts will combine to give an erroneous velocity measurement. In any case, the maximum allowable seeding particle density occurs when the 'next' particle is entering the measuring volume as the 'previous' particle is leaving. The maximum possible data rate is then given by the approximate relation:

$$\text{Maximum data rate} = \text{Local mean velocity} \div \text{Probe dimension}. \quad (3)$$

This maximum possible data rate is shown in figure 11 as a function of local mean velocity for the  $50\text{ }\mu\text{m}$  measuring volume used in this study.

Near the channel centreline, the local mean velocity is large, implying very high data rates. However, the intensity of the incident light is greatly reduced by scattering from the seed particles encountered in the fluid between the channel wall and the measuring volume. If the seeding particle density is high, the intensity of the

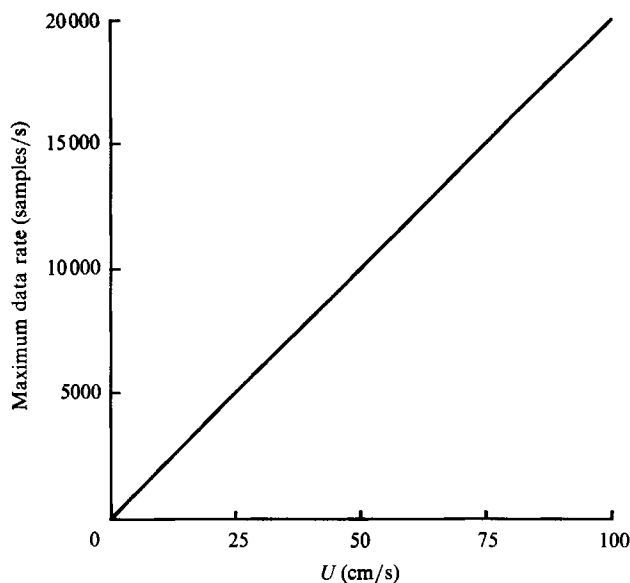


FIGURE 11. Maximum possible data rate for an ideal LDA with a 50  $\mu\text{m}$  measuring volume.

light scattered from seed particles in the measuring volume is low so that the signal-to-noise ratio of the photomultiplier signal is reduced and the data rate will be adversely affected. As the measuring volume is moved closer to the wall, the degree of attenuation of the incident light decreases because there is less seeded fluid between the channel wall and the measuring volume. There will be a range of  $y$ -locations where the flow velocities are large and the attenuation of light is small, resulting in larger signal-to-noise ratios and high data rates from the LDA.

Near the wall, a number of factors contribute to a significant reduction in the LDA data rate. First, the low mean streamwise velocities reduce the rate at which seeding particles are convected through the measurement volume. Secondly, the signal-to-noise ratio of the LDA photomultiplier signal is reduced by extraneous light scattered from the wall into the optical path leading to the photomultiplier. Additional reductions in data rate are caused by increases in both the intermittency and the magnitude of the velocity fluctuations relative to the mean velocity near the wall; the larger fluctuations reduce the data rate because of the LDA requirement that instantaneous  $U_1$  and  $U_2$  velocity measurements be between 0.2 and 1.8 times the component of the local mean velocity in the  $U_1$  or  $U_2$  direction. This criterion is described in §3.2.

Finally, a further reduction in data rate near the wall results from the fact that the magnitude of the transverse fluctuations relative to the mean velocity increases. There is then a higher probability of spanwise convection of a seed particle out of the measurement volume before eight fringes are crossed. Because of the simultaneity requirement imposed on the  $U_1$  and  $U_2$  measurements, if either one or both velocity measurements are lost from spanwise convection, the burst processor will reject the measurements; the data rate is reduced. A quantitative assessment of these additional contributions to the reduction in data rate near the wall has not been done. However, figure 12 clearly indicates that a significant reduction in data rate occurs near the wall.

The maximum data rates obtained at each  $y$ -location for all four Reynolds

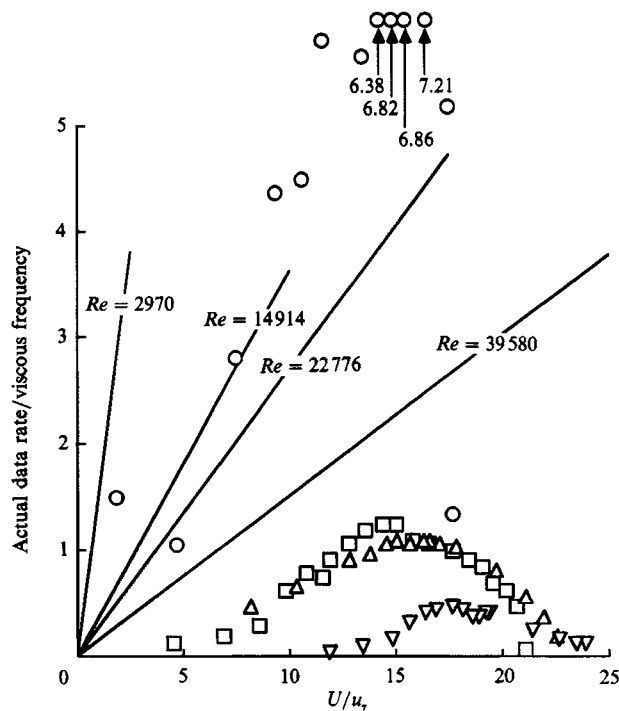


FIGURE 12. Data rate profiles, non-dimensionalized on inner variables, for the four Reynolds-number flows. The lines show the maximum possible data rates in an ideally seeded flow as a function of local mean velocity for the four Reynolds numbers of this investigation. The plotter symbols represent the following data:  $\circ$ ,  $Re = 2970$ ;  $\square$ ,  $Re = 14914$ ;  $\triangle$ ,  $Re = 22776$ ;  $\nabla$ ,  $Re = 39582$ . Note that the data rates are plotted versus  $u^+$  rather than  $y^+$ .

$Re$	Inverse timescale ( $u_\tau^2/\nu$ ) ( $s^{-1}$ )	Maximum data rate (samples/s)	Viscous length ( $\nu/u_\tau$ ) (cm)	Probe dimension in viscous lengths
2970	190	1400	0.0076	0.66
14914	3360	4200	0.0018	2.76
22776	5730	6300	0.0013	3.94
39580	11790	5400	0.0008	6.43

TABLE 1. Significant flow parameters for the four Reynolds-number runs

numbers appear in figure 12. These rates were non-dimensionalized with respect to the corresponding viscous frequencies. The maximum data rate for each profile is also presented in table 1 along with the viscous frequencies, and spatial resolution. Observe that the ordinate of figure 12 is the local mean (streamwise) velocity, non-dimensionalized by the friction velocity. This is analogous to plotting versus  $y^+$ . It may be seen from figure 12 that the highest data rates for the lower three Reynolds numbers were obtained in the range  $\sim 10 \leq u^+ \leq \sim 20$  ( $\sim 10 \leq y^+ \leq \sim 250$ ). For the lowest Reynolds number, the maximum data rate (for  $u^+ = 16$ ;  $y^+ = 92$ ) is over seven times greater than the viscous frequency. For the two intermediate Reynolds numbers, the maximum data rate is approximately equal to the viscous frequency, and the maximum data rate in the high Reynolds number case is less than half the viscous frequency.

The data rates for the three lowest Reynolds-number measurements in the range,  $\sim 10 \leq y^+ \leq \sim 250$ , were large enough to reconstruct the time-dependent velocity signals. Justification of this statement requires that one look ahead to the power spectra of the  $u$ ,  $v$ , and Reynolds-stress signals presented in figures 20, and 22–26. The non-dimensional ordinate,  $\Psi(\omega^+)$ , in each of these figures is defined in (10). The abscissa,  $\log[\omega^+]$ , is the logarithm (to the base 10) of angular frequency, non-dimensionalized by the viscous frequency. In these semi-log coordinates, the area under each of the spectra is proportional to the power in the velocity or Reynolds-stress fluctuations.

In order to determine accurately the contribution to the power spectrum of a random signal from a digital sample of the signal the sampling rate must be at least twice as great as the highest frequency component which contains significant power. If the sampling rate is below this sampling rate the power spectrum will be ‘aliased’; with the contributions to the total power from high-frequency components artificially ‘folded’ back to appear at lower frequencies. The average LDA data rate must therefore be high enough to prevent significant aliasing of the power spectrum. This will ensure that the digital LDA signal for the fluctuating velocity components contains all the ‘energetically’ significant velocity fluctuation information.

The lowest non-dimensional, average data rate for the various power spectra in figures 20 to 26 was  $\omega^+ = 3.75$  for the measurements at  $y^+ = 15.9$  and a Reynolds number of 22776 (see figure 12 for this data rate). For this case it can be observed in figures 20, 22 and 23 that there is very little power in the spectra of  $u$ ,  $v$ , and  $w$  above a frequency of half this average non-dimensional data rate for which  $\omega^+ = 3.75 \times \frac{1}{2} = 1.875$  and therefore  $\log(\omega^+) = \log(1.875) = 0.273$ . This shows that the average LDA data rate for the measurements at  $y^+ = 15.9$  and a Reynolds number of 22776 was sufficient to determine accurately the power spectra of the fluctuating velocity components without aliasing. As mentioned above, the average non-dimensional data rate for all the other spectral measurements was higher than the data rate for the measurements just discussed and from the plots of these spectra it can be observed that the amount of power in the spectra above the frequency corresponding to half these higher average non-dimensional data rates is negligible. From this, it is concluded that the reconstructed velocity traces for the three lowest Reynolds numbers were accurate representations of the actual velocity signals and the power spectra of figures 20–26 are valid because there is a negligible amount of power in the spectra at frequencies greater than half the average LDA data rate.

For the measurements at the highest Reynolds number,  $Re = 39580$ , the non-dimensional half data rate was  $\omega^+ = 0.05$ ,  $\log(\omega^+) = -1.3$ , at  $y^+ = 15$  and  $\omega^+ = 0.2$ ,  $\log(\omega^+) = -0.7$ , at  $y^+ = 130$ . These average data rates are too low to avoid aliasing of the power spectrum and therefore too low to allow accurate reconstruction of the velocity component fluctuations. However, the individual LDA measurements of the velocity for the highest Reynolds-number measurements are correct, but the location of the seed particle in terms of non-dimensional distance from the wall is more uncertain than for the lower Reynolds-number measurements. The data rates are so low that it is simply not possible to reconstruct the time-dependent velocity traces or to determine the power spectra of the fluctuations. It is still possible, however, to calculate accurate time averages of the velocity signals by employing a weighted averaging scheme.

Such a scheme, the velocity bias correction method, was devised by McLaughlin & Tideman (1973). The necessity for a correction arises because, assuming uniform seeding of the flow, the LDA data rate increases during high-speed (positive) velocity



fluctuations, and decreases during low-speed (negative) fluctuations. This results in more high-speed measurements than low-speed measurements. An ensemble average of these measurements produces a mean value which is biased high. To eliminate this bias, each individual velocity measurement is weighted by the inverse of the instantaneous velocity vector. This is discussed in greater detail by McLaughlin & Tiederman (1973) and by Wei (1987). The important point to note is that this correction is independent of the seeding density. As long as the flow is uniformly seeded, the velocity bias correction will provide correct time averages of the fluctuating quantities.

Resolution of a viscous timescale should not be equated with resolution of a viscous length scale. The small, intense shear layers observed by Willmarth & Bogar (1977) were less than 2.5 viscous lengthscales in size. Similar phenomena were observed by Willmarth and Sharma (1984) using even smaller hot-wire probes. However, the duration of the corresponding fluctuations in the hot-wire signal traces, shown in Willmarth & Sharma (1984), were on the order of ten viscous timescales.

As a closing note to this discussion of resolution, note that the straight lines appearing in figure 12 show the maximum possible data rate, non-dimensionalized on inner variables for each Reynolds number. That is, figure 11 has been reproduced in non-dimensional form for each of the four flow speeds. Comparison of the maximum possible data rates with the actual data rates shows that it should be possible, in principle, to significantly improve the performance of the LDA measurement system.

#### 4. Results

Non-dimensional mean velocity profiles,  $u^+$  vs.  $y^+$ , for four different Reynolds numbers are presented in figure 13. The solid line passing through the data represents the 'law of the wall' based on averages compiled by Coles (1953) for zero-pressure-gradient boundary layers. All the mean velocity profiles were fitted to this line by adjusting  $u_\tau$  and the wall location so that the experimental values of  $U/u_\tau$  and  $y^+$  agreed with the 'law of the wall'. Fitting the data to the 'law of the wall' provided a means of verifying the values of  $u_\tau$  calculated from the pressure gradient. In the three highest Reynolds-number cases, the values of  $u_\tau$  determined by fitting the centreline data to the 'law of the wall' agreed with the pressure gradient measurement of  $u_\tau$  to within 6%. In the lowest Reynolds number case,  $Re = 2970$ , the total pressure drop along the entire length of the channel was approximately 0.254 cm. In this case the pressure gradient was too small to be accurately measured with the instrumentation developed and available for this investigation. At the lowest Reynolds number, the only reliable way to determine  $u_\tau$  was by fitting the data to the 'law of the wall' profile compiled by Coles (1953).

Fitting the data to the 'law of the wall' also provided an accurate method of independently verifying the wall location. During each experimental run, the approximate wall location was found by moving the channel until the Mylar window intersected the measuring volume. When the LDA signal disappeared, it was assumed that the wall had been found. Once the mean velocity data far from the wall were fitted to the solid line (i.e. by adjusting  $u_\tau$ ), the data very near the wall were fitted by varying the origin of the  $y$ -coordinate representing the wall location. This could be done without appreciably changing the data farther from the wall. In all four cases, the required adjustment of the origin was less than 0.0076 cm or 1.5 times the LDA measurement volume diameter.

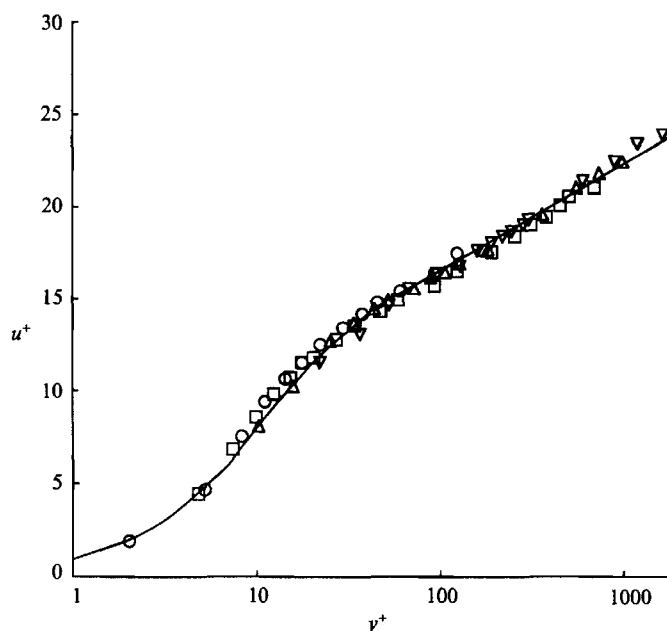


FIGURE 13. Mean velocity profiles, non-dimensionalized on inner variables, for the four Reynolds numbers examined.  $\circ$ ,  $Re = 2970$ ;  $\square$ ,  $Re = 14914$ ;  $\triangle$ ,  $Re = 22776$ ;  $\nabla$ ,  $Re = 39582$ . The solid line through the data is the 'law of the wall' plot compiled by Coles (1953) for a zero-pressure-gradient turbulent boundary layer.

The 'law of the wall' also provides a control against which the present data could be compared. It is important to observe here that the measured mean velocity profiles scale with inner variables and are consistent with previous investigations. Significant deviations from the solid line would have indicated the presence of non-uniformity in the mean flow field in the channel.

The turbulence intensity measurements are shown in figures 14 and 15. In figure 14, the  $u'$  and  $v'$  profiles are non-dimensionalized with respect to the local average streamwise velocity,  $U$ , and plotted against  $y^+$ . Non-dimensionalization by the local streamwise velocity describes the intensity of the turbulent fluctuations relative to the square root of the mean kinetic energy per unit mass at a given distance from the wall. Note that the  $v'/U$  measurements approaching the wall exhibit an apparent increasing trend for all four Reynolds numbers. This is not possible because from the continuity equation,  $\partial v/\partial y = 0$ , at the wall. It is believed that this inconsistency is caused by reduced measurement resolution very close to the wall. A more complete discussion of the measurement uncertainties is presented in Wei (1987).

The  $u'$  and  $v'$  turbulence intensity profiles were also scaled on inner variables and appear in figure 15. For comparison with relevant data from the literature, the reader is referred to figures 1 and 2. There is good agreement between the present data and that of Eckelmann (1974), Johansson & Alfredsson (1982), and Laufer (1950). The measured maximum values of  $u'/u_\tau$  agree with the data in the literature to within 5%. There is noticeably less agreement at the higher two Reynolds numbers. The maximum values in Laufer's (1950) highest Reynolds-number data,  $Re = 61600$ , differ from the present measurements by more than 25%. As discussed in §1.1, this is probably due to the decreased spatial resolution of the hot-wire probes used by Laufer (1950), and also by Comte-Bellot (1965) and Johansson & Alfredsson (1982).

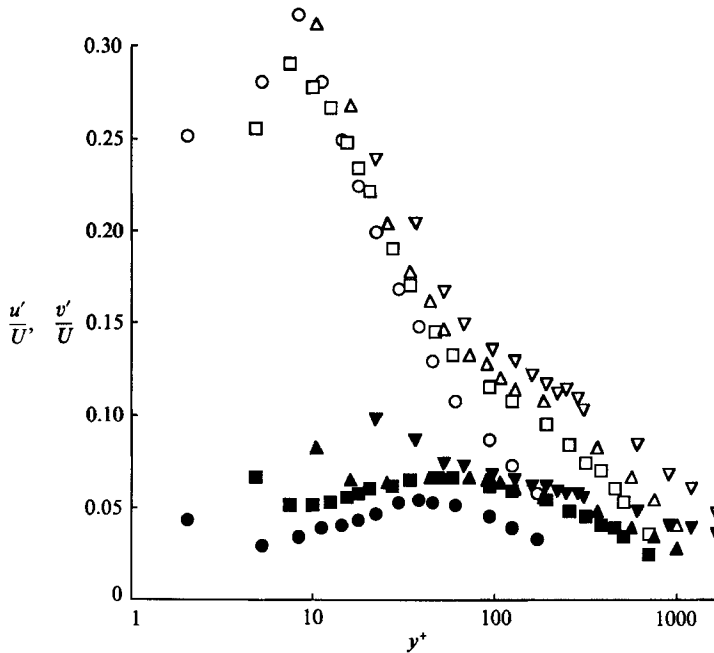


FIGURE 14. Profiles of the turbulence intensity in the stream direction,  $u'$  (open points), and the direction normal to the wall,  $v'$  (solid points), non-dimensionalized on the local mean velocity.  $\circ$ ,  $Re = 2970$ ;  $\square$ ,  $Re = 14914$ ;  $\triangle$ ,  $Re = 22776$ ;  $\nabla$ ,  $Re = 39582$ . This figure illustrates a possible Reynolds-number effect and resolution problems close to the wall.

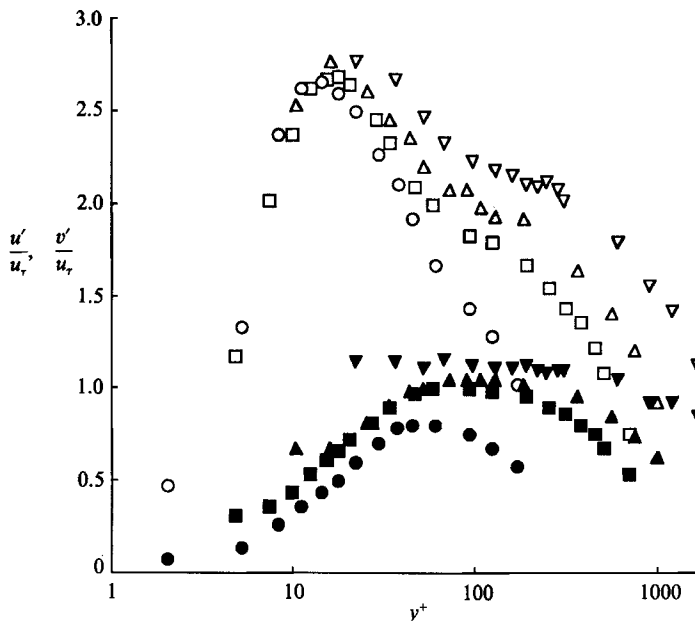


FIGURE 15. Streamwise and normal turbulence intensity profiles, non-dimensionalized on inner variables, for all four Reynolds-number flows.  $\circ$ ,  $Re = 2970$ ;  $\square$ ,  $Re = 14914$ ;  $\triangle$ ,  $Re = 22776$ ;  $\nabla$ ,  $Re = 39582$ . The open symbols represent the streamwise measurements,  $u'$ , and the solid symbols represent the component normal to the wall,  $v'$ .

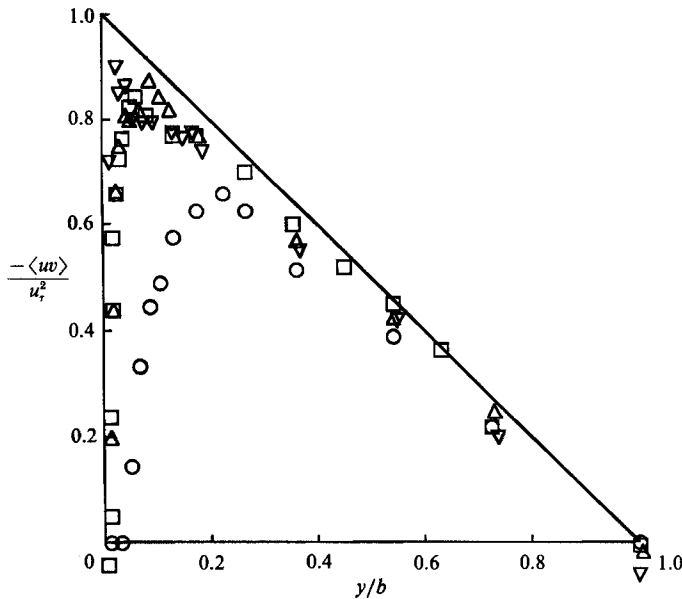


FIGURE 16. Reynolds stress profiles for all four Reynolds-number flows.  $\circ$ ,  $Re = 2970$ ;  $\square$ ,  $Re = 14914$ ;  $\triangle$ ,  $Re = 22776$ ;  $\nabla$ ,  $Re = 39582$ . The solid line represents the total shear stress profile.

The Reynolds-stress measurements, normalized with the friction velocity and plotted versus  $y/b$ , are shown in figure 16. These measurements will be referred to as the 'direct Reynolds-stress measurements'. They were obtained by averaging the product of the measured  $u$  and  $v$  velocity fluctuations. Data from the literature are shown in figure 17 for comparison. The advantages of using a high-resolution LDA are again evident from the fact that the only previous Reynolds-stress measurements very close to the wall, where the Reynolds stress is decreasing, were made with hot-film probes by Eckelmann (1974) at very low Reynolds number.

It is worth noting that the maxima of the non-dimensional Reynolds-stress profiles increase in magnitude and are closer to the wall as the Reynolds number increases. Since the maximum value of the non-dimensional Reynolds stress is not the same for each profile, the Reynolds-stress profiles do not scale with inner variables in the Reynolds-number range investigated. This may be seen more clearly in figure 18, where the 'direct' non-dimensional Reynolds-stress profiles are plotted as functions of  $y^+$ .

The solid lines in figure 18 are the normalized Reynolds-stress profiles calculated from the momentum balance equation using measurements of the pressure gradient and the mean velocity profiles. These solid-line profiles will hereinafter be referred to as the 'momentum balance' Reynolds-stress measurements. This independent measurement of the Reynolds stress using the momentum equation provides a good test of the accuracy of the direct Reynolds-stress measurements and a further, independent check that the reconstructed velocity traces used for the direct Reynolds-stress measurements were valid.

The equation for the momentum balance determination of the Reynolds stress is obtained from the mean momentum equation:

$$\rho \left( \frac{DU_i}{Dt} \right) = - \left( \frac{\partial P}{\partial x_i} \right) - \rho \left( \frac{\partial \langle u_i u_j \rangle}{\partial x_j} \right) + \mu \left( \frac{\partial^2 U_i}{\partial x_j^2} \right). \quad (4)$$

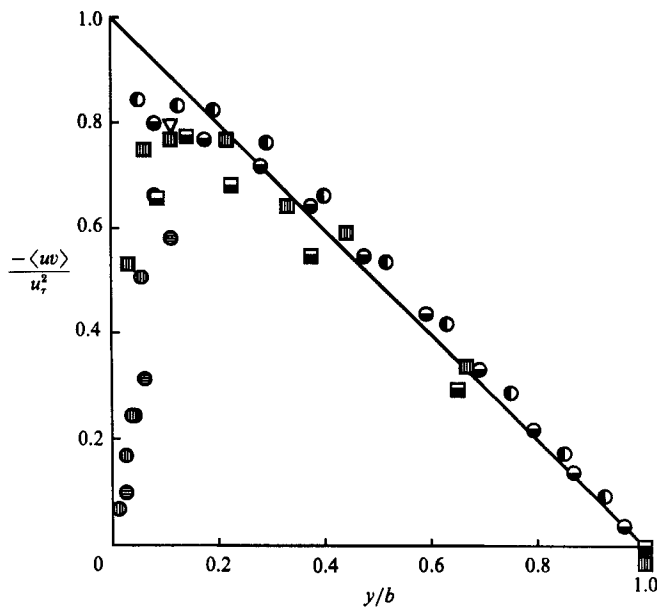


FIGURE 17. Reynolds-stress profiles reproduced from the turbulent channel flow literature:  $\bullet$ ,  $Re = 2800$  (Eckelmann 1974);  $\bullet$ ,  $Re = 4100$  (Eckelmann 1974);  $\blacksquare$ ,  $Re = 7500$  (Alfredsson & Johansson 1984);  $\blacksquare$ ,  $Re = 12600$  (Kastrinakis & Eckelmann 1983);  $\bullet$ ,  $Re = 57000$  (Comte-Bellot 1965);  $\bullet$ ,  $Re = 230000$  (Comte-Bellot 1965).

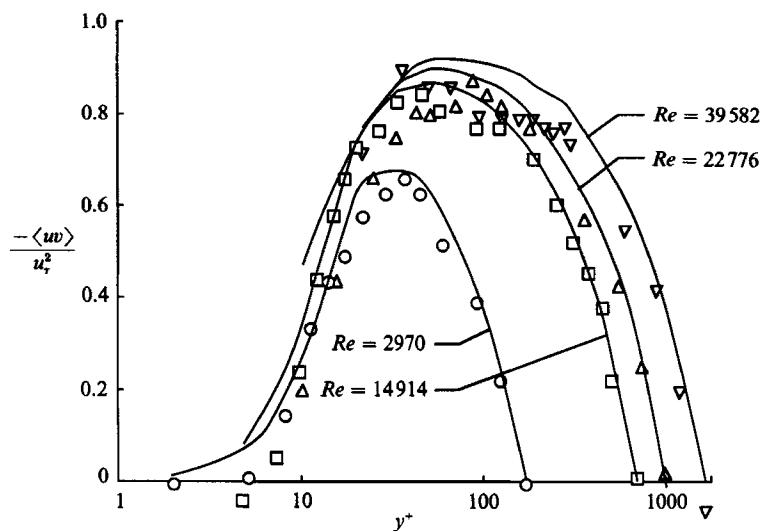


FIGURE 18. Reynolds-stress profiles, non-dimensionalized on inner variables, for the four Reynolds-number flows.  $\circ$ ,  $Re = 2970$ ;  $\square$ ,  $Re = 14914$ ;  $\triangle$ ,  $Re = 22776$ ;  $\nabla$ ,  $Re = 39582$ . The open symbols represent the directly measured values and the solid lines represent the momentum balance calculations.



For a fully developed, two-dimensional turbulent channel flow, there are no mean velocity or Reynolds stress variations in the  $x$ - or  $z$ -directions, the flow is not accelerating, and  $V = W = 0$ . The pressure varies only in the  $x$ -direction. Upon substitution, (let the subscripts 1, 2, and 3 correspond to the  $x, y$ , and  $z$ -directions, respectively), the  $x$ -momentum equation is:

$$0 = -\left(\frac{dP}{dx}\right) - \rho \left(\frac{d\langle uv \rangle}{dy}\right) + \mu \left(\frac{d^2 U}{dy^2}\right). \quad (5)$$

Since  $dP/dx$  is a constant in a fully developed turbulent channel flow, this equation may be integrated once with respect to  $y$ . Application of the boundary conditions (i.e. at the centre of the channel,  $y = b$ , both the Reynolds stress and  $dU/dy$  are zero) yields:

$$\rho \langle uv \rangle = (b - y) dP/dx + \mu (dU/dy). \quad (6)$$

At the wall,  $y = 0$ , there is no Reynolds stress and the wall shear stress determined from the above equation is:

$$\mu (dU/dy)_w = \rho u_\tau^2 = -b(dP/dx). \quad (7)$$

After introducing this relation and writing the equation in non-dimensional form, the streamwise momentum equation yields the following equation for the Reynolds stress:

$$-\langle uv \rangle / u_\tau^2 = \{1 - (y/b)\} - dU^+ / dy^+. \quad (8)$$

Equation (8) was used to generate the Reynolds-stress profiles shown as solid lines in figure 18. The friction velocity was determined from (7) using the measured pressure gradient, and  $dU/dy$  was determined from a second-order polynomial fitted through seven points of the mean profile, centred at the  $y$ -location in question. The polynomial was then differentiated at the central point. This process was repeated along the entire velocity profile. Since there were insufficient data to obtain accurate near-wall derivatives for the higher two Reynolds numbers, the non-dimensional velocity profile compiled and tabulated by Coles (1953) was used. In the two lower Reynolds-number cases, the agreement between the direct and the momentum balance Reynolds-stress measurements is better than 10% except for the data at small  $y^+$ . This is probably due to spatial and temporal resolution problems in the direct LDA measurement very close to the wall. At the next highest Reynolds number,  $Re = 22776$ , the directly measured values fall off sharply from the momentum balance Reynolds-stress curve for  $y^+$  less than approximately 70. The directly measured Reynolds-stress value at  $y^+ = 10.3$  is nearly 60% lower than the momentum balance calculated value. This indicates that the resolution limitations of the LDA were affecting a significant portion of the inner region.

When the data rate is lower than that necessary to properly reconstruct the fluctuating velocity the statistical properties will be in error. It was possible to calculate the long-time statistics using the velocity bias correction techniques, developed by McLaughlin & Tiederman (1973), for the ensemble averages of the original measured velocities (see § 3.4). This was done for all four Reynolds numbers. The results for the ensemble averages of the original data with velocity bias correction were compared with the ensemble averages from the reproduced/filtered/smoothed velocity signals. In the three lower Reynolds-number flows, the agreement between the two different methods for the local mean stream velocity,  $U$ , was better than 2%. Agreement for the mean Reynolds stress and all of the root-mean-square statistics was better than 5%, except near the wall. For the highest

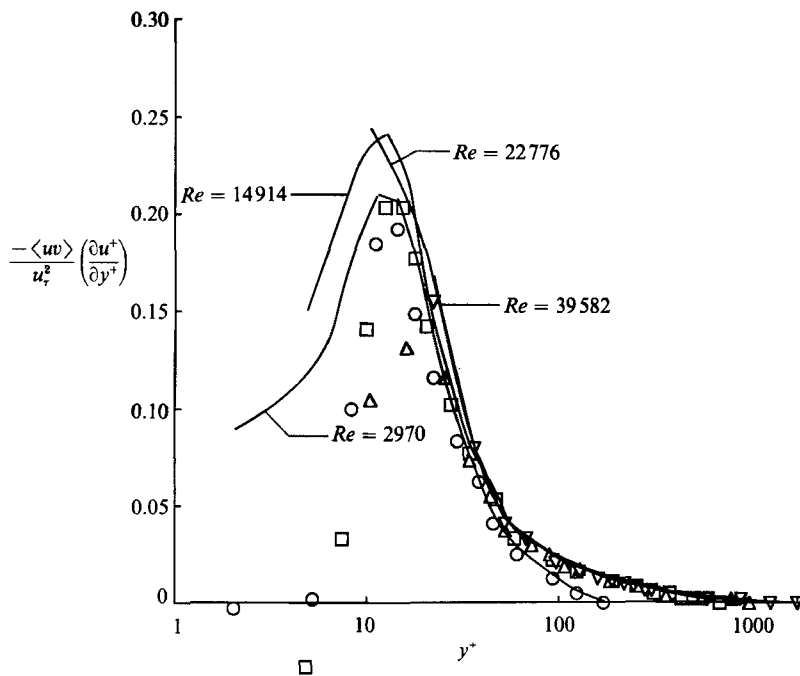


FIGURE 19. Turbulent kinetic energy production profiles including direct measurements (open points) and momentum balance calculations (solid lines).  $\circ$ ,  $Re = 2970$ ;  $\square$ ,  $Re = 14914$ ;  $\triangle$ ,  $Re = 22776$ ;  $\nabla$ ,  $Re = 39582$ .

Reynolds number, the magnitudes of mean Reynolds stress and the second moments, calculated using the two different averaging methods, differed by as much as 15%. The calculations of  $U$  differed by 3%. Thus, at the highest Reynolds number, results obtained using the original data with the velocity bias correction were used. This applies to all of the high-Reynolds-number data presented in this paper.

The turbulent kinetic energy production profiles were calculated from the Reynolds stress and  $dU/dy$  measurements. They are shown in figure 19, non-dimensionalized on inner variables. The plot symbols were generated by multiplying the direct Reynolds stress measurements by  $dU/dy$ . The solid lines were generated by multiplying the momentum balance Reynolds-stress values by  $dU/dy$ .

The agreement between the directly measured production values and the values obtained using the momentum balance Reynolds-stress measurements for the two lower Reynolds numbers is generally within 10%. However, like the Reynolds-stress measurements, the directly measured data diverge from the solid lines near the wall. As stated above, this is believed to be related to the inadequate resolution of the LDA very close to the wall.

## 5. Discussion

The results of this investigation indicate that the fluctuating quantities in the inner region of a turbulent channel flow do not scale with inner variables between the Reynolds numbers of 2970 and 39580. This is readily apparent from the turbulence intensity profiles appearing in figure 15. It can be seen that  $u'/u_\tau$  scales on inner variables only up to  $y^+ = 12$  which is well inside the inner region. The  $v'/u_\tau$  profiles

do not scale on inner variables anywhere in the channel. In general, in the Reynolds-number range of this investigation, the turbulent fluctuations, non-dimensionalized on inner variables, become larger in amplitude with increasing Reynolds number.

Figures 18 and 19 show that the Reynolds-stress and kinetic-energy-production profiles also do not scale on inner variables. The Reynolds-stress profiles, shown in figure 18, become broader with increasing Reynolds number. This stems from the fact that, in terms of viscous lengths, the channel centreline is farther away from the wall at higher Reynolds numbers. Since the mean Reynolds stress in a channel flow is zero only at the channel walls and the centreline, necessarily the Reynolds stress profile, when plotted against  $y^+$ , becomes broader.

Of greater physical significance is the fact that the maximum normalized Reynolds-stress values increase with Reynolds number. At low Reynolds numbers, the flow is laminar, and there is no Reynolds stress anywhere in the channel. As the Reynolds number increases, transition from laminar to turbulent flow occurs. Randomly oriented vorticity appears in the flow, giving rise to Reynolds stresses. At  $Re = 2970$ , the maximum value of the  $-\langle uv \rangle / u_\tau^2$  profile is 0.66, while the maximum value of  $-\langle uv \rangle / u_\tau^2$  is approximately 0.90 in the highest Reynolds-number profile,  $Re = 39582$ . As the Reynolds number increases, it is believed that the maximum values of the normalized Reynolds-stress profiles will continue to increase. The limiting case, as the Reynolds number approaches infinity, is that  $-\langle uv \rangle / u_\tau^2$  cannot exceed unity; a mean normalized Reynolds-stress value greater than unity in a fully developed turbulent channel flow would violate the conservation of momentum.

The kinetic-energy-production profiles also appear to demonstrate a Reynolds-number effect. For the three lower Reynolds numbers, the maximum values of the momentum balance calculated profiles, shown as solid lines in figure 19, appear to increase in magnitude with increasing Reynolds number. At the highest Reynolds number, it was not possible to obtain data close enough to the wall to resolve the maximum value of the production. A stronger statement regarding the Reynolds-number dependence of the production profiles requires a larger number of data points in the range,  $5 \leq y^+ \leq 30$ , to better resolve the maxima.

It is hypothesized that these Reynolds-number dependences are caused by changes in the coherent structure of the turbulence close to the wall. Examination of the time-dependent velocity signals led to the conclusion that there are two phenomena which are responsible for the observed Reynolds-number effects. The first phenomenon is the enhancement of the vortex-stretching mechanism in the inner region with increasing Reynolds number. The second effect is the interaction of the inner region structure from opposing walls, particularly at low Reynolds number. These two phenomena will be discussed in §5.2 and §5.3, respectively.

### 5.1. *The coherent structure in the inner region*

It has been proposed that the inner region is comprised of an array of hairpin vortices aligned in the stream direction. Use of the hairpin vortex model in this paper is supported by the following experimental measurements and observations of turbulent wall-bounded flows. The hairpin model was first hypothesized by Theodorsen (1955). A decade later, Tu & Willmarth (1966) found that the hairpin vortices were useful in explaining hot-wire and pressure transducer measurements made in a zero-pressure-gradient turbulent boundary layer.

Around this time, visual investigations using hydrogen-bubble flow-visualization techniques were initiated by Hama & Nutant (1963). They observed that transition to turbulent flow began with the production of a hairpin-shaped vortical structure

which emerged from the region near the wall and rapidly evolved, ultimately resulting in a random chaotic motion. The success of this initial visual observation led to further studies in fully-developed turbulent flow including that of Kline *et al.* (1967).

Kline *et al.* (1967) used the hydrogen-bubble flow-visualization technique in a free-surface water channel. They found that a randomly occurring process, now known as the turbulent burst, was the dominant flow process in the turbulent boundary layer. They hypothesized that this process involved a hairpin-vortex structure and showed that most of the Reynolds stress is produced during this bursting process.

As mentioned in §1.1, Head & Bandyopadhyay (1981) observed coherent rotational fluid in the near-wall region of very high Reynolds-number boundary layers. These structures were observed using smoke visualization in a wind tunnel. Head & Bandyopadhyay (1981) concluded that the structures were hairpin vortices and observed that the number of hairpin structures increased with increasing Reynolds number.

The concept of a hairpin vortex was incorporated into the work of Perry & Chong (1982). They used a  $\Lambda$ -shaped vortex model to describe the coherent turbulent structure in the inner region of a zero-pressure-gradient boundary layer. Their analysis provided a reasonably accurate prediction of the mean turbulence quantities. Further, they demonstrated that the mean velocity profile may be satisfactorily described by an hierarchical array of these vortices. This hierarchy was qualitatively similar in appearance to the visualization study of Head & Bandyopadhyay (1981).

Numerical investigations of the near-wall structure of fully developed turbulent channel flows also indicate the existence of a hairpin vortical structure in the inner region. Moin & Kim (1985) conditionally sampled the instantaneous vorticity fields generated using numerical methods in the near-wall region of a low-Reynolds-number turbulent channel flow. They found that the isovorticity lines tended to coalesce into horseshoe-shaped patterns. They drew the same conclusion, that the inner region was dominated by hairpin (or horseshoe) vortices.

### 5.2. The effect of increased vortex stretching

To gain further insight into the inner region turbulence structure, it is important to consider the vorticity field. This field is mathematically described by the vorticity equation. Conventional thought holds that the inner region should scale only on inner variables. The vorticity equation should then be non-dimensionalized on inner variables. However, in so doing, the non-dimensional vorticity equation will exhibit no Reynolds-number dependence. It has already been demonstrated that the inner region of a turbulent channel flow exhibits a Reynolds-number dependence over the Reynolds-number range of this investigation. Since the Reynolds number is a dimensionless grouping of outer variables, failure of the turbulence quantities in the inner region to scale only on inner variables is an indication that the dynamics of the inner region structure are affected by outer as well as inner variables. Therefore, it is reasonable to examine the inner region dynamics using the velocity equation, non-dimensionalized on outer variables:

$$D\mathbf{\Omega}^*/Dt^* = (\mathbf{\Omega}^* \cdot \nabla^*) \mathbf{u}^* + Re^{-1}(\nabla^{*2} \mathbf{\Omega}^*), \quad (9)$$

where  $\mathbf{\Omega}$  represents vorticity and the asterisk superscript denotes a quantity made dimensionless using outer variables,  $b$  and  $U_{\text{centreline}}$ . Equation (9) states that the total rate of change of vorticity following a fluid particle is due to the combined effects

of vortex stretching or compression and viscous diffusion. Observe that the coefficient of the diffusion term is inversely proportional to the Reynolds number and is the only term in the equation that explicitly depends on Reynolds number.

Although the Reynolds number appears in the denominator of the diffusion term of (9) one cannot neglect the diffusion of vorticity in the vicinity of solid boundaries in a turbulent flow. Lighthill (1963) points out that at high Reynolds numbers, fluid motions in a whole range of scales become unstable. This implies that in turbulent flow, motions of smaller scale can extract energy from motions of larger scale. Near the wall this cascade process has the effect of bringing the turbulent vorticity fluctuations in closer contact with the wall, while the vortex lines are more and more stretched. Ultimately, the fluctuating vorticity reaches a region near the wall where the gradients have become so intense that the diffusion of vorticity counteracts the effect of further stretching. Lighthill (1963) further points out that the wall is also a source of new vorticity which is generated by mean of fluctuating pressure gradients. Thus, the diffusion term is of great importance at all Reynolds numbers in a turbulent flow near solid boundaries.

It is believed that the Reynolds-number effects demonstrated in this investigation arise because, as Reynolds number increases, the inner-region vorticity field is stretched to a degree greater than that dictated by inner scaling laws. This implies a natural evolution from low-Reynolds-number turbulence to high-Reynolds-number turbulence. In terms of the hairpin vortex model, the legs of the hairpins are increasingly stretched at higher Reynolds numbers which results in smaller diameter vortex cores with greater vorticity concentrated in the cores. It is suggested that the turbulent flow structure at high Reynolds number near solid boundaries (i.e. the hairpin-vortex structure and interactions) will differ significantly from lower-Reynolds-number turbulent-flow structure; there is a natural evolution of the structure of wall-dominated turbulence from low Reynolds number to high Reynolds number.

One way to test this hypothesis is to examine the power spectra of the fluctuating velocity signals at different Reynolds numbers. Smaller hairpin vortices with greater vorticity in the cores should appear in the velocity signals as larger-amplitude fluctuations of shorter period which contribute to the high-frequency range of the power spectrum. Recall that the area under the power-spectrum of a fluctuating velocity signal is proportional to the mean kinetic energy of that velocity component. Thus the power spectra of the fluctuating velocity signals, non-dimensionalized with respect to inner variables, should then exhibit greater 'energy' content at high frequencies with increasing Reynolds number.

This effect of Reynolds number on the stretching of vorticity in the inner region is apparent in the power spectra of the velocity and Reynolds-stress fluctuations for the three lower Reynolds-number flows in the vicinity of the kinetic energy production peak ( $10 \geq y^+ \leq 5$ ), shown in figures 20–23. The spectra of the normalized velocity and Reynolds-stress fluctuations are presented in the format used by Perry & Abell (1975) in their paper on scaling laws for pipe-flow turbulence. The ordinate of the spectra,  $\Psi(\omega^+)$ , is defined so that the area beneath a semi-logarithmic plot of the spectra, as displayed in figures 20, and 22–26, is the mean-square of the velocity of the Reynolds-stress fluctuations divided by friction velocity to the second or fourth power (for the velocity and Reynolds-stress spectra, respectively). The relation between  $\Psi(\omega^+)$  and the power spectral density of the velocity or Reynolds-stress fluctuations,  $\Phi(\omega^+)$ , is:

$$\Psi(\omega^+) = \omega^+ \Phi(\omega^+) / \nu. \quad (10)$$



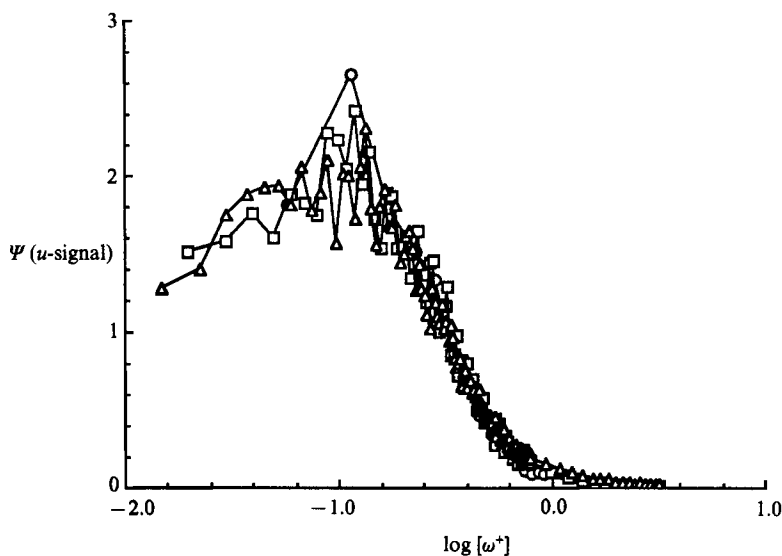


FIGURE 20. Power spectra of the streamwise velocity signals near  $y^+ = 15$  for the three lower Reynolds-number flows.  $\circ$ ,  $Re = 2970$ ;  $\square$ ,  $Re = 14914$ ;  $\triangle$ ,  $Re = 22776$ .  $\Psi$  is the product of the angular frequency and the power spectrum, non-dimensionalized on inner variables (see text);  $\omega^+$  is the non-dimensional angular frequency.

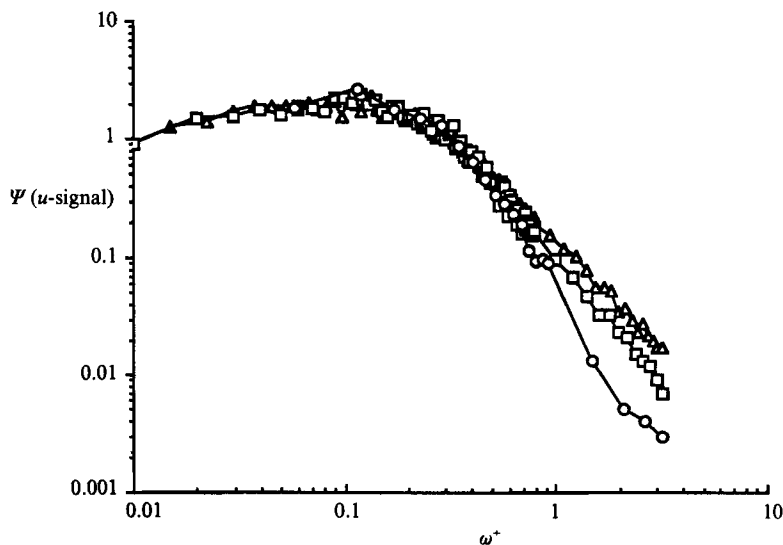


FIGURE 21. The same streamwise power spectra as those presented in figure 20. In this figure, the spectra are plotted on a log-log scale.

In (10),  $\omega^+ = \omega\nu/u_\tau^2$  is the radian frequency scaled with inner variables. A subscript  $u$ ,  $v$ , or  $uv$ , is used in figures 20–26 for the power spectra of these fluctuating quantities.

Power spectra taken in the near-wall region, around  $y^+ = 15$ , appear in figures 20–23. Each spectrum is an ensemble average of at least fifty individual 1024 point realizations of signal traces, reproduced at even time intervals. The traces were generated from the raw data traces at twice the average data rate. The Gaussian

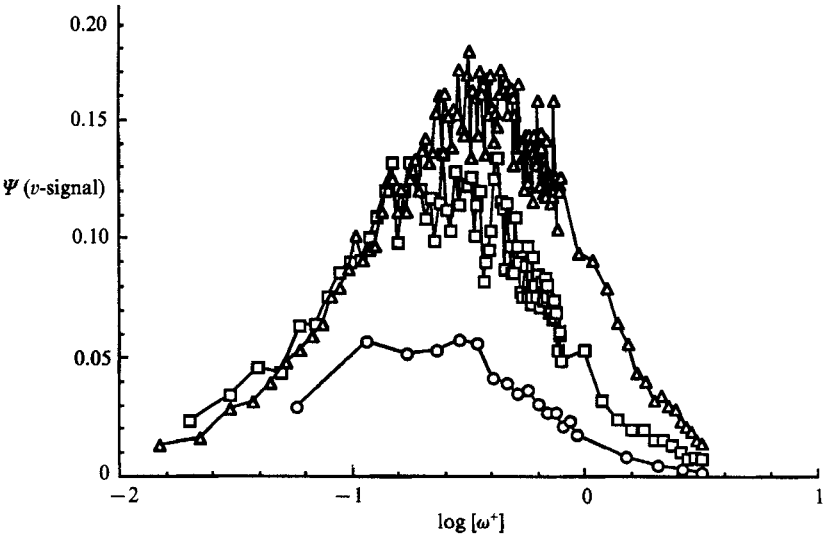


FIGURE 22. Power spectra of the normal velocity signals near  $y^+ = 15$  for the three lower Reynolds-number flows. (See figure 20 for legend and explanation of the axes.)

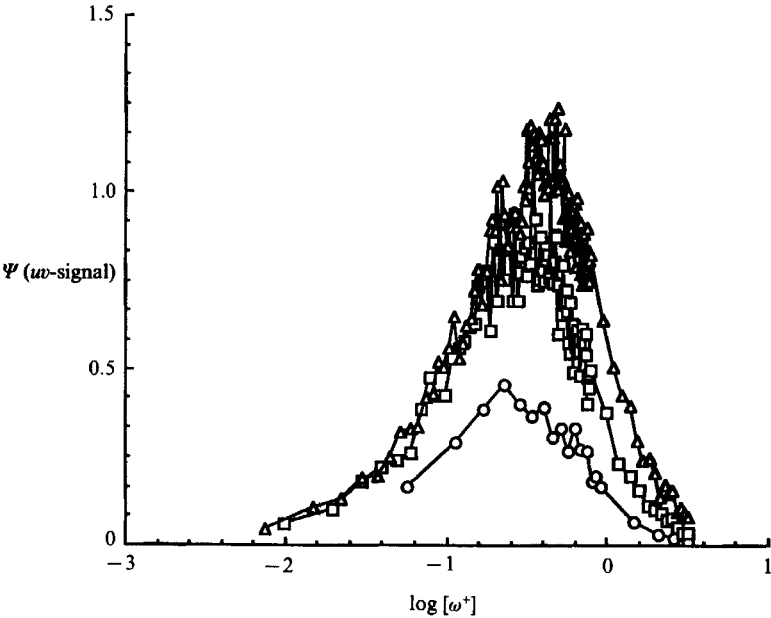


FIGURE 23. Power spectra of the Reynolds-stress signals near  $y^+ = 15$  for the three lower Reynolds-number flows. (See figure 20 for legend and explanation of the axes.)

digital filter for each trace was set with the half power point at a frequency corresponding to twice the viscous frequency (i.e.  $\omega^+ = 2.0$ ). This ensured that the effect of the filter was outside the energy-containing frequency range. Reconstruction at twice the data rate was done in an attempt to ensure that all of the intermittent high-frequency contributions were included in the spectra. A few of the power spectra were computed from traces generated at the average data rate and showed

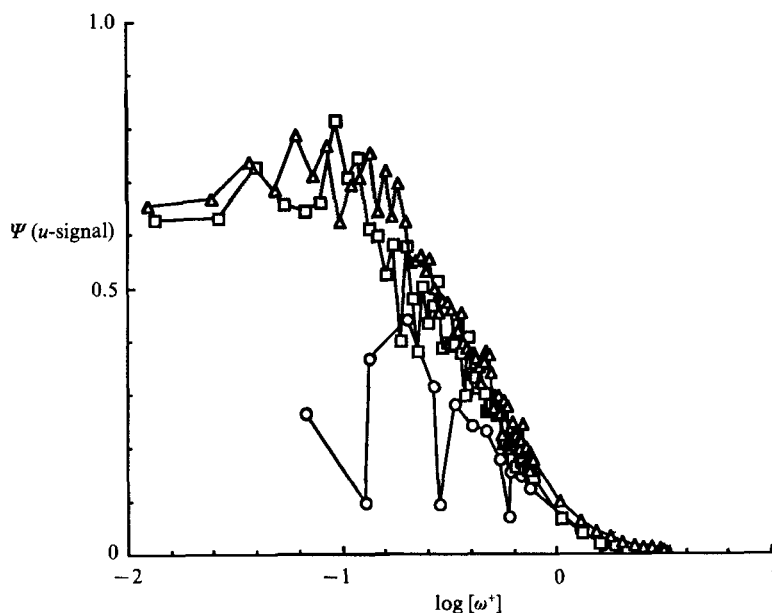


FIGURE 24. Power spectra of the streamwise velocity signals near  $y^+ = 125$  for the three lower Reynolds-number flows. (See figure 20 for legend and explanation of the axes.)

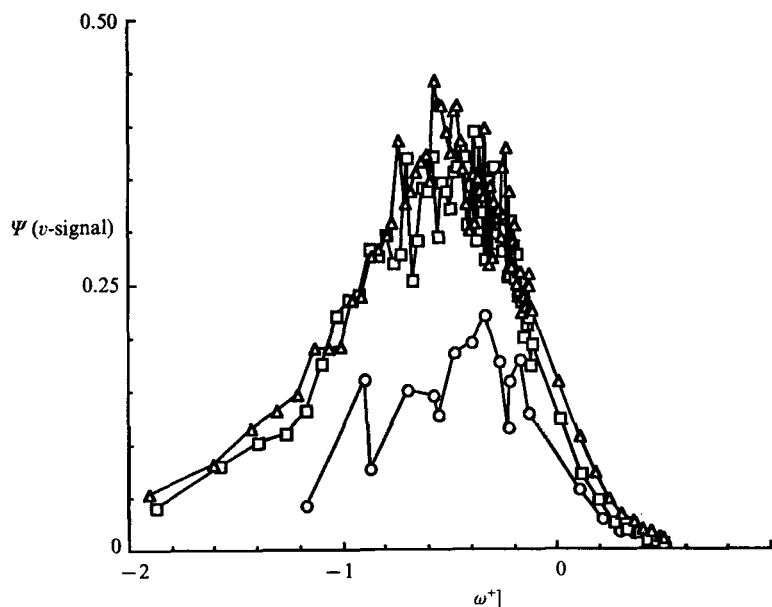


FIGURE 25. Power spectra of the normal velocity signals near  $y^+ = 125$  for the three lower Reynolds-number flows. (See figure 20 for legend and explanation of the axes.)

no appreciable difference in the spectra. Additional information about the power spectrum algorithm may be found in Wei (1987).

Figures 20 and 21 show the  $u$ -power spectra for the conditions described in the previous paragraphs. There is appreciable scatter at lower frequency, but generally the  $u$ -power spectra indicate that the lower frequency, energy-containing eddies

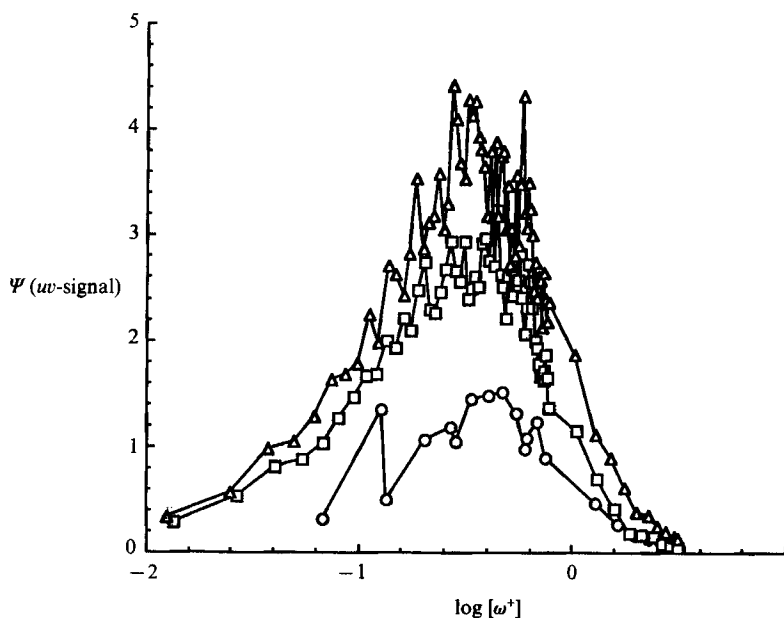


FIGURE 26. Power spectra of the Reynolds-stress signals near  $y^+ = 125$  for the three lower Reynolds-number flows. (See figure 20 for legend and explanation of the axes.)

scale on inner variables. The behaviour of these spectra at high frequency (where the energy in the spectrum is low) are more clearly displayed in figure 21 in which the ordinate is  $\Psi$  plotted on a logarithmic scale. The three spectra begin to diverge at  $\omega^+ = 0.4$  ( $\log [\omega^+] = -0.4$ ). In the non-dimensional frequency range,  $0.4 < \omega^+ < 1.0$  ( $-0.4 \leq \log [\omega^+] \leq 0$ ), there is greater energy at the high frequencies with increasing Reynolds number. Because these high frequencies correspond to smaller eddies, this demonstrates that in non-dimensional terms, smaller eddies appear at higher Reynolds number which is consistent with the notion of increased vortex stretching at higher Reynolds numbers.

The increase in the streamwise kinetic energy with increasing Reynolds number is very slight since the energy in the frequency range

$$0.4 < \omega^+ < 1.0 \quad (-0.4 \leq \log [\omega^+] \leq 0)$$

is small. Thus, near  $y^+ = 15$  the effect of vortex stretching is visible in the  $u$ -power spectra, but is not readily apparent in the  $u'/u_\tau$  measurements. Indeed, for  $y^+ \leq 12$ , the  $u'/u_\tau$  data in figure 15 appear to scale with inner variables.

The  $v$ -power spectra near the wall, presented in figure 22, do not scale on inner variables over a large portion of the energy-containing frequency range. Like the  $u$ -spectra, the three spectra diverge with increasing values of  $\omega^+$ , but at much lower frequencies. While the two higher-Reynolds-number spectra appear to scale for  $\log \omega^+ \leq -1$  ( $\omega^+ \leq 0.1$ ), the lowest-Reynolds-number spectrum does not intersect or overlap the other spectra at any point. Observe that at any non-dimensional frequency,  $\omega^+$ , in the range,  $-1 \leq \log \omega^+ \leq 0.5$  ( $0.1 \leq \omega^+ \leq 3.0$ ), the value of  $\Psi$  for the  $Re = 14914$  spectrum is nearly 2.5 times the value of  $\Psi$  at  $Re = 2970$ . This is consistent with the observation that the  $v'/u_\tau$  profiles do not scale on inner variables even very close to the wall.

The power spectra of the time-dependent Reynolds-stress signals near the wall, depicted in figure 23, closely resemble the  $v$ -power spectra just discussed. This is

consistent with the fact that the Reynolds-stress fluctuations are the product of  $u$  and  $v$ . Since the  $u$ -power spectrum appear to scale on inner variables up to quite high frequencies, the  $uv$  and  $v$ -power spectra should be similar, particularly at lower frequencies.

Kim, Kline & Reynolds (1971) used flow-visualization methods to demonstrate that essentially all of the Reynolds stress in a turbulent boundary layer was produced during the bursting time in the zone near the wall,  $0 < y^+ < 100$ . The Reynolds-number range of their investigation, based on outer variables (i.e. free-stream velocity and boundary-layer thickness), was  $5550 < Re_\delta < 10645$ . This approximately coincides with the lowest two Reynolds-number cases,  $Re = 2970$  and  $14914$ , covered in this investigation. In this Reynolds-number range, the results of Kim *et al.* (1971) indicate that the Reynolds stress and associated fluctuations are produced by intermittent velocity fluctuations during the bursting time; between bursts there is little Reynolds stress. One can therefore associate the lack of inner scaling of both the Reynolds-stress fluctuations and the  $v$ -velocity fluctuations with the lack of scaling on inner variables of the process responsible for the generation of the Reynolds stress during bursting. As previously suggested, it is believed that this process is essentially the intermittent process of stretching of hairpin vortices.

Since the velocity gradient decreases with increasing distance from the wall, the stretching of the fluctuating vorticity field by the mean flow decreases with increasing distance from the wall. It is therefore expected that the power spectra taken at  $y^+ = 125$ , corresponding to the outer limit of the inner region, should demonstrate some high-frequency Reynolds-number dependence. However, owing to the diminished stretching of vorticity farther away from the wall, this effect will be weaker than that found in the spectra measured close to the wall.

The streamwise and normal power spectra for the three lower Reynolds numbers near  $y^+ = 125$  are shown in figures 24 and 25. Both figures exhibit Reynolds-number effects at the high frequencies. However, as expected, comparison of figures 20 and 22 with figures 24 and 25 respectively show that the Reynolds-number effect is stronger close to the wall. Comparison of the Reynolds-stress spectra at  $y^+ = 15$  and at  $y^+ = 125$ , shown in figures 23 and 26, yields the same conclusion.

It may be observed that the low-frequency range of the spectra at  $y^+ = 125$ , shown in figures 24–26, does not scale with inner variables. This is consistent with the measurements of Bradshaw (1967) who hypothesized that the lack of scaling at low frequencies was due to large scale ‘inactive’, essentially irrotational motions in the outer region. This may be thought of as low frequency ‘sloshing’ of the outer region fluid.

The concept of increased stretching of the hairpin vortices with increasing Reynolds number is useful in explaining the Reynolds-number effects observed in the time-averaged quantities shown in figures 15 and 18. As the Reynolds number increases, there is an increase of vorticity in the legs of the hairpin vortices. Very close to the wall the legs of the hairpin vortices are essentially aligned parallel to the wall. The induced velocities would therefore be primarily normal to the wall. As the Reynolds number increases a stationary probe, located very close to the wall, would detect larger  $v$ -fluctuations as the hairpin vortices are convected past the probe. It is not clear that equally large  $u$ -fluctuations would be detected. This is consistent with the results shown in figure 15 where, for  $y^+ \leq 12$ , the non-dimensional streamwise turbulence intensity profiles scale on inner variables and do not change with Reynolds number, but the non-dimensional  $v$ -fluctuations do not scale on inner variables and increase with increasing Reynolds number.

Further away from the wall, the hairpin-vortex legs rise from the wall and connect to the vortex heads. Between the legs, there is an induced flow in the negative  $u$ -direction and in the positive  $v$ -direction. Increased stretching of the vortices as the Reynolds number increases has a direct effect on the fluctuations in both  $u$  and  $v$ . In the range,  $15 \leq y^+ \leq 100$ , it would be expected that neither component of turbulence intensity,  $u'$  nor  $v'$ , would scale on inner variables. This result is readily observed in figure 15, since the non-dimensional turbulent intensities increase with Reynolds number in the range,  $15 \leq y^+ \leq 100$ .

Increases in the strength of both  $u$ - and  $v$ -fluctuations resulting from the stretching of vortices also result in increased Reynolds stress fluctuations. If a hairpin were to pass directly over a stationary probe so that the legs of the hairpin straddle the sensor, the probe will detect a decrease in  $u$  and an increase in  $v$ . If the hairpin passes to either side of the probe, the fluctuations will be reversed. In either event, this corresponds to negative contributions to  $\langle uv \rangle$ . The magnitudes of the Reynolds-stress fluctuations, non-dimensionalized on inner variables, would increase with Reynolds number as dictated by the increased stretching of the vorticity field. In the relatively quiescent periods between the passage of hairpin vortices, there is little Reynolds stress. Thus, increased stretching of the hairpin vortices causes the magnitude of the local average Reynolds stress to be larger. This would explain why the maxima of the Reynolds-stress profiles, shown in figure 18, increase with Reynolds number. It also agrees with the idea that there must be a Reynolds-number range in which the non-dimensional Reynolds-stress maximum evolves from zero, in the laminar-flow case, and approaches some value not greater than unity, in the infinite-Reynolds-number case.

An argument in favour of inner scaling at high Reynolds numbers can be made with the aid of the Reynolds-stress plot shown in figure 16. It was pointed out in §4 that the maxima of the non-dimensional Reynolds-stress profiles increase and move closer to the wall with increasing Reynolds number. In the limit of infinite Reynolds number the pressure gradient, which drives the flow in the channel, is balanced everywhere by turbulent momentum exchange except in a very thin region near the wall. At very high Reynolds number, the Reynolds-stress profiles should closely approach the solid line in figure 16, except, of course, in the thin region near the wall where the Reynolds stress must be zero and viscous forces are dominant.

At high Reynolds numbers, the Reynolds-stress profiles will be very close to the infinite Reynolds-number profile. An increase in Reynolds number will no longer significantly change the Reynolds-stress profiles. The physical interpretation is that the process of vortex stretching in the inner region is no longer a function of Reynolds number. At these high Reynolds numbers, it is possible that inner scaling of the mean and fluctuating quantities will exist.

### 5.3. *The effect of channel geometry*

The interaction of turbulence from opposing walls has been observed in previous investigations which were motivated by the desire to understand when and how a channel or pipe flow becomes fully developed. Patel (1974) and Reynolds (1974) reported that the mean and fluctuating velocity profiles in a turbulent pipe indicate that the flow is not fully developed until as many as 50–80 pipe diameters downstream of the inlet. This was true in spite of the fact that the pressure gradient was constant and appeared to indicate that the flow was fully developed 10–20 diameters from of the inlet.

Dean & Bradshaw (1976) verified that there was significant interaction of



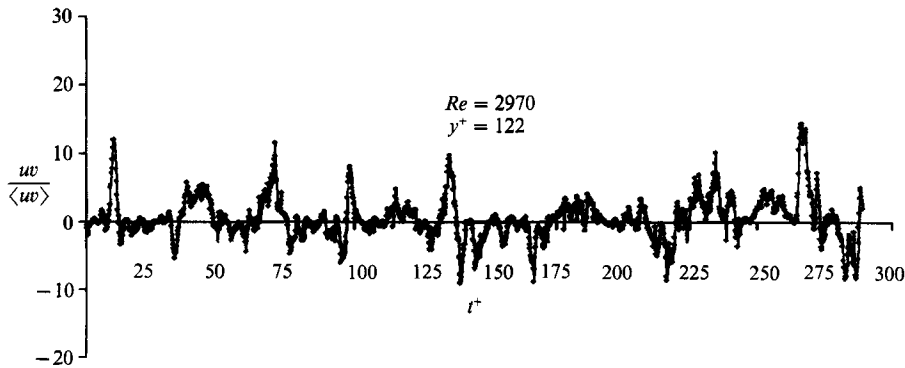


FIGURE 27. Sample time-dependent Reynolds-stress trace at the lowest Reynolds number,  $Re = 2970$ , and  $y^+ = 122$  ( $y/b = 0.726$ ). The abscissa is non-dimensionalized on the viscous timescale, and the ordinate is non-dimensionalized on the mean Reynolds stress.

structures from opposing walls. By heating the fluid on one side of a rectangular channel, they were able to observe that fluid from opposite walls regularly crossed the centreline. They found that the flow did not become fully developed until the interaction reached an asymptotic state.

A fully developed turbulent channel flow may loosely be thought of as two boundary layers placed back to back which are continually interacting. From symmetry, the velocity gradient,  $dU/dy$ , and the Reynolds stress,  $-\rho\langle uv \rangle$ , must be zero at the centreline. At the lowest Reynolds number examined in this investigation,  $Re = 2970$ , the dimensionless channel half-width is only 170 viscous lengths. This places the channel centreline barely outside the inner region of either wall; there really is no outer region in this flow.

In this low-Reynolds-number turbulent flow, a turbulent burst occurring at one wall may extend well across the centreline to the far wall. Bursts from either wall would then regularly extend into the inner region of the opposing wall. Since the mean spanwise vorticity from one wall is oriented in a direction opposite to the vorticity at the other wall, the two walls constantly exchange counter-rotating fluid between their respective inner regions. This is what will be referred to as the 'geometry effect'.

For the highest-Reynolds-number flow, the centreline of the channel was 1655 viscous lengths from the wall. Consequently, a large percentage of the channel was occupied by the outer region. It should be expected that the degree of interaction between the inner regions of the two walls would be less than in the low-Reynolds-number case.

In this investigation, evidence of the geometry effect at low Reynolds numbers appears in the time-dependent Reynolds stress traces. Figures 27 and 28 are sample traces at the lowest,  $Re = 2970$ , and higher intermediate,  $Re = 22776$ , Reynolds numbers, respectively. The instantaneous  $uv$  measurements are non-dimensionalized with respect to the appropriate long-time averaged values. Note that non-dimensionalizing the individual  $uv$  products by the local mean Reynolds stress inverts the trace; negative contributions to  $\langle uv \rangle$  appear above the time axis. The time is non-dimensionalized on viscous units. The lower-Reynolds-number trace was recorded 122 viscous length from the wall, corresponding to  $y/b = 0.726$ . The higher-Reynolds-number trace was reconstructed from data taken 127 viscous lengths from the wall. However, in the latter case, this corresponded to  $y/b = 0.126$ .

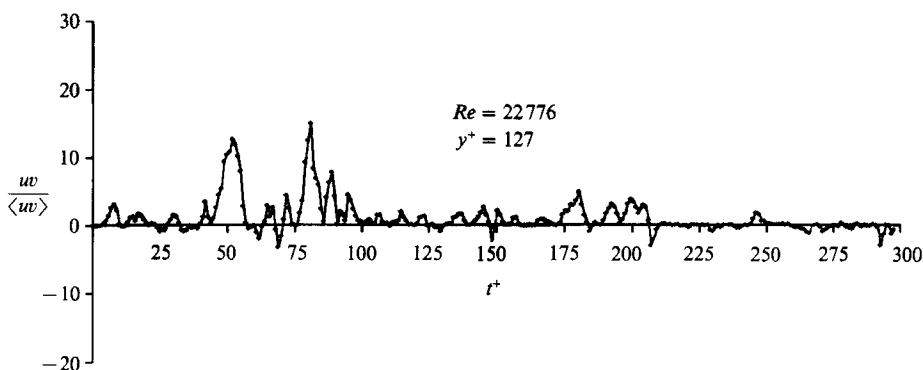


FIGURE 28. Sample Reynolds-stress trace at  $Re = 22776$ , and  $y^+ = 127$  ( $y/b = 0.126$ ). The abscissa is non-dimensionalized on the viscous timescale, and the ordinate is non-dimensionalized on the mean Reynolds stress. Observe the qualitative differences between figures 27 and 28.

There are a large number of both positive and negative Reynolds-stress fluctuations in figure 27. This indicates that, at that location, the probe is sensing bursting events from both channel walls. The mean Reynolds stress value is small,  $-\langle uv \rangle / u_\tau^2 = 0.220$ , because the contributions, of opposite sign, from both walls cancel each other over time. At low Reynolds numbers, therefore, the Reynolds stress at the channel centreline is zero not because there are no Reynolds-stress fluctuations there, rather, the fluctuations from both walls cancel each other in a statistical sense over time.

In contrast, the higher-Reynolds-number trace in figure 28, at  $y^+ = 127$  and  $y/b = 0.126$ , has more negative fluctuations than positive ones. The mean value of  $-\langle uv \rangle / u_\tau^2$  is 0.817. Individual large amplitude fluctuations are signatures of passing bursts from one wall only. There is little evidence of bursts from the far wall affecting the inner region at the higher Reynolds numbers which would appear as large positive-amplitude Reynolds-stress fluctuations.

#### 5.4. Additional comments

There are a number of ramifications of these results on current channel-flow research. First, practically all of the channel-flow research performed to date was conducted within the Reynolds-number range covered by this investigation. As pointed out in §1.1, virtually all of these investigators have assumed, *a priori*, the existence of a Reynolds-number-independent inner scaling. It may be necessary to reassess many of the conclusions which were drawn using the inner-scaling assumption.

Secondly, very close to the wall, probe resolution is a critical problem. Laufer's (1950) data, in particular, demonstrate the loss of spatial resolution in X-wire measurements with increasing Reynolds number. At his highest Reynolds number, Laufer's X-wire probe was approximately 25 viscous units in length. The spacing between wires was probably also large. One can see that the maximum values of his turbulence-intensity profiles decrease with increasing Reynolds number. This contradicts physical reasoning, and is contrary to the results of this investigation.

Willmarth & Bogar (1977) demonstrated that an X-wire probe does not work properly if the wires are immersed in a flow with small-scale regions of very high shear. In such flows, the two wires will often sense different parts of the local shear region. The assumption that the X-wire is immersed in a locally uniform flow field is not valid.

The LDA used in this study does not suffer from that problem. One may actually think of the probe as the seeding particle itself. The LDA measurement of the particle velocity, assuming the settings of the burst detection apparatus are correct, is a true representation of the flow velocity in the immediate vicinity of the particle. In this case, the average spatial resolution of the 'probe' was 3  $\mu\text{m}$ . The spatial resolution of the LDA is limited by the inability to determine the exact location of the particle inside the measurement volume. This is very different from the X-wire problem, where one has limited confidence in not only the spatial location of the measurement, but of the measurement itself.

Clearly, the Reynolds-number effects demonstrated in this study are not caused by the decrease in spatial resolution with increasing Reynolds number. The data from the literature demonstrates that the loss of spatial resolution with increasing Reynolds number results in values of the root-mean-square velocity-fluctuation measurements which are too low. This investigation demonstrates that the maximum values of the turbulence intensity profiles increase with increasing Reynolds number. Therefore, the Reynolds-number effect cannot be attributed to probe resolution problems. In fact, it is believed that the non-dimensional probe size of this LDA at the higher Reynolds numbers was significantly smaller than any probe used to date.

Finally, this study indicates that there are fundamental differences between the turbulent flows in a circular pipe, a rectangular channel, and a zero-pressure-gradient boundary layer. It was observed that in the channel flow, the inner-region structure from the opposing walls interacted. There was a constant interchange of counter-rotating vorticity between the two inner regions due to bursting. There cannot be a similar phenomenon occurring in a boundary layer because there is only one wall. The circular pipe flow will be more complex. The curvature of the pipe wall means that the inner-region structure from different circumferential locations can interact at the centre of the pipe. Clearly, the resulting turbulent structure of the three-flow geometries will be different.

## 6. Conclusions

High-resolution, two-component LDA measurements were made in a fully developed turbulent channel flow over a Reynolds-number range of 3000 to 40000. The data rates obtained were sufficiently high to reconstruct the time-dependent velocity signals. From these reconstructed signals, the time-averaged mean and fluctuating quantities were calculated. Critical examination of these results led to the following conclusions:

- (i) Inner scaling laws of the fluctuating quantities in the inner region are Reynolds-number dependent over the range examined.
- (ii) Near the wall, at  $y^+ = 15$ , power spectra of the streamwise velocity fluctuations appear to scale with inner variables over most of the energy-containing frequency range.
- (iii) However, at the same  $y^+ = 15$  location, spectra of the velocity fluctuations normal to the wall and the fluctuating Reynolds stress do not scale on inner variables in the energy-containing frequency range.
- (iv) The lack of inner scaling is primarily due to increased stretching of the inner-region vorticity field in the stream direction.
- (v) There is also a geometry effect whereby the inner-region structure from opposing channel walls interact, particularly at lower Reynolds numbers.

The support of this work by the Office of Naval Research through Dr Michael Reischman is gratefully acknowledged.

## REFERENCES

- ALFREDSSON, P. H. & JOHANSSON, A. V. 1984 On the detection of turbulence-generating events. *J. Fluid Mech.* **139**, 325–345.
- BLACKWELDER, R. F. & HARITONIDIS, J. H. 1983 Scaling of the bursting frequency in turbulent boundary layers. *J. Fluid Mech.* **132**, 87–103.
- BRADSHAW, P. 1967 ‘Inactive’ motion and pressure fluctuations in turbulent boundary layers. *J. Fluid Mech.* **30**, 241–258.
- CLAUSER, F. H. 1956 The turbulent boundary layer. *Adv. Applied Mech.* **4**, 1–51.
- COLES, D. 1953 Measurements in the boundary layer on a smooth flat plate in supersonic flow; Part I. the problem of the turbulent boundary layer. *JPL/Cal Tech Rep.* no. 20–69.
- COLES, D. 1956 The law of the wake in the turbulent boundary layer. *J. Fluid Mech.* **1**, 191–226.
- COMTE-BELLOT, G. 1965 Ecoulement turbulent entre deux parois paralleles. *Publications Scientifiques et Techniques du Ministère de l’Air* no. 419.
- DEAN, R. B. & BRADSHAW, P. 1976 Measurements of interacting turbulent shear layers in a duct. *J. Fluid Mech.* **78**, 641–676.
- ECKELMANN, H. 1974 The structure of the viscous sublayer and the adjacent wall region in a turbulent channel flow. *J. Fluid Mech.* **65**, 439–459.
- ERM, L. P., SMITS, A. J. & JOUBERT, P. N. 1985 Low Reynolds number turbulent boundary layers on a smooth flat surface in a zero pressure gradient. *Fifth Symp. on Turbulent Shear Flow, Cornell University*, **2**, 13–18.
- HAMA, F. R. & NUTANT, J. 1963 Detailed flow-field observations in the transition process in a thick boundary layer. *Proc. of the 1963 Heat Transfer and Fluid Mech. Institute* (ed. A. Roshko, B. Sturtevant & D. R. Bartz), pp. 77–93. Stanford University Press.
- HEAD, M. R. & BANDYOPADHYAY, P. 1981 New aspects of turbulent boundary-layer structure. *J. Fluid Mech.* **107**, 297–338.
- JOHANSSON, A. V. & ALFREDSSON, P. H. 1982 On the structure of turbulent channel flow. *J. Fluid Mech.* **122**, 295–314.
- JOHANSSON, A. V. & ALFREDSSON, P. H. 1983 Effects of imperfect spatial resolution on measurements of wall-bounded turbulent shear flows. *J. Fluid Mech.* **137**, 409–421.
- JOHNSON, F. D. & ECKELMANN, H. 1983 Has a small-scale structure in turbulence been experimentally verified? *Phys. Fluids*, **26**, 2408–2414.
- KASTRINAKIS, E. G. & ECKELMANN, H. 1983 Measurement of streamwise vorticity fluctuations in a turbulent channel flow. *J. Fluid Mech.* **137**, 165–186.
- KIM, H. T., KLINE, S. J. & REYNOLDS, W. C. 1971 The production of turbulence near a smooth wall in a turbulent boundary layer. *J. Fluid Mech.* **50**, 133–160.
- KLINE, S. J., REYNOLDS, W. C., SCHRAUB, F. A. & RUNSTADLER, P. W. 1967 The structure of turbulent boundary layers. *J. Fluid Mech.* **30**, 741–773.
- KREPLIN, H. P. & ECKELMANN, H. 1979 Behavior of the three fluctuating velocity components in the wall region of a turbulent channel flow. *Phys. Fluids*, **22**, 1233–1239.
- LAUFER, J. 1950 Investigation of turbulent flow in a two-dimensional channel. *NACA Tech. Note* TN2123.
- LIGHTHILL, M. J. 1963 Introduction. Boundary Layer Theory. In *Laminary Boundary Layers* (ed. L. Rosenhead). Oxford University Press.
- LUCHIK & TIEDERMAN, W. G. 1986 Effect of spanwise probe volume length on laser velocimeter measurements in wall bounded turbulent flows. *Exp. Fluids* **3**, 339–341.
- LUMLEY, J. L. & PANOFKY, H. A. 1964 *The Structure of Atmospheric Turbulence*. Interscience.
- McLAUGHLIN, D. K. & TIEDERMAN, W. G. 1973 Biasing correction for individual realization of laser anemometer measurements in turbulent flows. *Phys. Fluids*, **16**, 2082–2088.
- MOIN, P. & KIM, J. 1985 The structure of the vorticity field in a turbulent channel flow. Part 1. Analysis of instantaneous fields and statistical correlations. *J. Fluid Mech.* **155**, 441–464.

- PATEL, R. P. 1974 A note on fully developed turbulent flow down a circular pipe. *Aeronaut J.* **78**, 93–97.
- PERRY, A. E. & ABELL, C. J. 1975 Scaling laws for pipe flow turbulence. *J. Fluid Mech.* **67**, 257–271.
- PERRY, A. E. & CHONG, M. S. 1982 On the mechanism of wall turbulence. *J. Fluid Mech.* **119**, 173–217.
- PURTELL, L. P., KLEBANOFF, P. S. & BUCKLEY, F. T. 1981 Turbulent boundary layer at low Reynolds number. *Phys. Fluids.* **24**, 802–811.
- REYNOLDS, A. J. 1974 *Turbulent Flows in Engineering*. John Wiley.
- SCHWE, G. 1983 On the structure and resolution of wall-pressure fluctuations associated with turbulent boundary-layer flow. *J. Fluid Mech.* **134**, 311–328.
- THEODORSEN, T. 1955 The structure of turbulence. *50 Jahre Granzschichtforschung* (ed. H. Görtler, & W. Tollmien). Braunschweig, Vieweg.
- TU, B. J. & WILLMARTH, W. W. 1966 An experimental study of the structure of turbulence near the wall through correlation measurements in a thick turbulent boundary layer. *The University of Michigan Dept of Aerospace Engng Rep.* 02920-3-T.
- WEI, T. 1987 Reynolds number effects on the small scale structure of a turbulent channel flow. PhD thesis, Dept. of Aerospace Engng The University of Michigan.
- WILLMARTH, W. W. & BOGAR, T. J. 1977 Survey and new measurements of turbulent structure near the wall. *Phys. Fluids. suppl.* **20**, S9–S21.
- WILLMARTH, W. W. & SHARMA, L. K. 1984 Study of turbulent structure with hot wires smaller than the viscous length. *J. Fluid Mech.* **142**, 121–149.
- WILLMARTH, W. W. & VELAZQUEZ, J. S. 1983 High resolution laser-doppler anemometer for turbulence measurements in a channel. *8th Biennial Symp. on Turbulence at the Univ. of Missouri – Rolla, Sept. 1983*, pp. 18.1–18.12.